APPLICATIONS OF THE AVE-SESAME DATA SETS TO MESOSCALE STUDIES

A REPORT

from the space science and engineering center
the university of wisconsin-madison
madison, wisconsin

APPLICATIONS OF THE AVE-SESAME DATA SETS TO MESOSCALE STUDIES

FINAL REPORT

David Suchman, Principal Investigator
Brian Auvine
H. Michael Goodman
Raymond Lord
David Santek

Space Science and Engineering Center
The University of Wisconsin-Madison
Madison, WI 53706

June 1983

Final Report on NASA Contract NAS8-33799

Table of Contents

1. Introduction

This report deals with the progress made in the past two and one-half years in applying the AVE-SESAME data sets to mesoscale studies with particular emphasis on satellite applications. This work is a logical outgrowth of two other satellite-oriented programs at SSEC, one dealing with GATE (Suchman, et al., 1981), and the other with mid-latitude systems (Suomi, 1980).

The purpose of this program was twofold: (1) to produce more complete and meaningful data sets by combining rapid-scan GOES imagery with conventional observations from the AVE-SESAME experiment; and (2) to study small-scale characteristics of severe thunderstorms and their environment by using the above mentioned data sets. Our experience had been that satellite data had shown us things not observed by conventional data, but alone, the picture was a limited one. The same was true for radar or radiosonde or surface measurements. But, if one could combine radar and satellite images, or rawinds with cloud drift winds, research possibilities were greatly enhanced.

The program plan was as follows: to investigate the quantitative applications of GOES data, complemented by conventional data, to study the structure and dynamics of severe local storms and convective outbreaks. In pursuing this plan, our work was divided into three general areas of concentration: (1) the improvement of methods whereby rapid-scan satellite imagery could be combined with conventional meteorological observations to produce more useful data sets. This included improvements in cloud-tracking and analysis techniques for deriving better mesoscale wind fields, and combining maps of digital satellite and radar brightness maps to elucidate small-scale thunderstorm and convective features; (2) the use of

satellite brightness data to isolate deep convection and to detect severe weather in its incipient stages; and (3) the investigation of small-scale thunderstorm characteristics including the relation of cold domes and overshooting tops (number, strength, and movement) to severe weather at the surface.

Although we do not have as much case study work as we had hoped, we have made much progress in all the above areas. This report is organized by subject area: data, data processing, and data products; cloud winds; small-scale storm features; severe weather-satellite brightness relationships; anvil statistics; and software improvements.

2. Data

Our original intention was to perform three complete case studies of days from SESAME '79. One would be a day with weak activity (June 8), one with intermediate (May 20), and one with strong activity (May 2). Unfortunately, the situations were far from ideal, and no day presented us with a complete data set covering the life cycle of the severe weather producing storms; hence we had to settle for bits and pieces of two of the days, without the opportunity for a complete case study. May 2 had good convective activity and satellite coverage, but the radar was far from ideal in areal coverage. On the other hand, the radar for May 20 was of good quality, though the weather was not as active. The work presented will, therefore, be a combination of those two days.

A second problem was data accessibility. Though we had access to SSEC's satellite archive, the rest of the data was slow in coming and, in some cases, had to be checked very carefully.

Data were gathered from many sources and were reformatted to McIDAS (Man-computer Interactive Data Access System) compatible files to allow integration and intercomparison of data sets with existing software. Table 1 summarizes the data acquired and the types of files used. The Station Data Set (SDS) files, RAOB files, and image files are stored on tape that can be easily restored on the McIDAS.

All data contained in SDS files or RAOB files can be plotted on the terminal graphics in Mercator projection (with base map) or over a satellite image. The data can also be interpolated to a rectangular latitude-longitude grid [through a Barnes (1973) objective analysis] and contoured (or streamlines drawn for wind) in Mercator or satellite projection.

The digital radar images are initially read into image files, each scan line in the file corresponding to one radial of radar data. These intermediate images serve as a beginning point for remapping to satellite projection or RHI sections.[1] CAPPI's[2] are generated from a series of radar images at different elevation angles. Areas of beam overlap are averaged. Because of the wide beam width (2°), CAPPI's should not be used where echoes of interest are more than 100 km from the radar site. RHI images were made at a specified radial at a number of elevation angles. The resolution along the radial direction was good (1 km), but the vertical resolution degraded to 7 km at 200 km range. All remapping used bilinear spline interpolation.

---

[1] RHI: Range Height Indicator

[2] CAPPI: Constant Altitude Plan Position Indicator

Type	Source	Dates	McIDAS Format
Portable Automated Mesomet (PAM)	FSU	2, 20 May	SDS file
Aircraft (Sabreliner, QueenAire)	NCAR	2 May	SDS file
Severe Weather Reports	SESAME Operations Manual	2, 20 May	SDS file
RAOB	SSEC archive	2, 20 May	RAOB file
RAOB Meso Network	NSSL, MSFC	2, 20 May	RAOB file
Digital Radar	NSSL	2, 20 May	Image Save Tape
Satellite	SSEC archive	2, 20 May, 8 June	Image Save Tape

FSU: Florida State University
NCAR: National Center for Atmospheric Research
SSEC: Space Science and Engineering Center
NSSL: National Severe Storms Lab
MSFC: Marshall Space Flight Center
SDS: Station Data Set

Table 1. Data Sources

To overlay the radar or station data on the satellite image, an offset due to parallax was added in. In the central USA, viewing from GOES-East, this amounts to about 1 km in the horizontal for each kilometer in height. Radar CAPPI's and SDS files were also saved on tape with a parallax adjustment.

In order to enable us to use the satellite images to their fullest, these images were often brightness normalized. Brightness normalization refers to a process whereby satellite digital brightness data are changed to values that would be sensed by the satellite at a specified reference point and time to correct for changing solar and satellite viewing angles. These adjustments rely heavily on the consistency of the data in both space and time. However, the normalization procedure does pose several problems that may affect data integrity.

The relationship between satellite sensed brightness and solar angle is closely approximate to a trigonometric sine curve function for small zenith angles only. Thus, for times close to local noon, corrections for sun angle change can be made with a fair degree of accuracy. Because the earth-to-satellite viewing angle does not change appreciably for a geostationary satellite, this factor may be neglected. One should be aware, however, that spatial variation of atmospheric cloud features themselves can cause local inaccuracies. In order to obtain relatively consistent corrections, normalization assumes the cloud feature to be of fixed thickness and infinite lateral extent.

The assumption fails to account for the edges of cloud features where a contrast in brightness is assumed. Within a cloud, textured areas (i.e., cluster of turrets or domes) may also reveal differences in areal maximum brightness for changing solar angles from a shadowing effect. The shapes

and sizes of the clouds, and, on a smaller scale, differing concentrations and sizes of water droplets will create brightness differences that will be sensed by the satellite and be inherent in the data.

For more information relating to data processing, see Section 7 on Software Improvements.

3. Mesoscale Wind Sets

This portion of the study included the generation of mesoscale sets of cloud tracer winds, integration of these winds with other existing wind data, and the use of these data sets as part of our examination of the severe local storm environment. Toward this end we obtained wind sets for both 2120 GMT and 2314 GMT, May 2, 1979. The first cells on this day appeared around 1930 GMT; the first severe weather was reported at 2020 GMT, continuing on into the early morning hours. Thus both wind set times fell within the period of vigorous cell growth and activity. Later wind set times could not be attempted because of the loss of visible satellite data after about 0000 GMT, May 3. The area of analysis was centered at around 36°N, 98°W extending over 10° of latitude by 15° of longitude.

The procedures followed were like those outlined in Suchman et al. (1981). Visible and infrared GOES images at 6 minute intervals (with an additional image on either side to aid continuity) were looped and used for tracking by single pixel techniques (the motions of a cursor were adjusted manually until it moved along with an operator selected cloud feature). To aid in discriminating fine detail, various black and white enhancements were applied to the image brightnesses. Full resolution (1 km nominal) data was used in the immediate vicinity of the storm where most of the low level tracers lay; the remainder of the area was tracked using 2 km data.

Initial heights were assigned to the tracers on the basis of Mosher's (1976) cloud height algorithm and the use of moisture information from NWS and NSSL soundings in the area. Later, groups of vectors with similar motions were interactively compared with winds from these same soundings to help in editing and assigning a final height. Tracer winds that differed substantially from both the sounding winds and nearby tracers of the same or proximate cloud layers were rejected.

In general, the cloud tracers agreed well with the soundings and grouped themselves into 8 levels ranging from 925 mb to 250 mb. Most of the vectors (numbering 214 vectors at 2120 and 252 at 2314 GMT) were found from 250 to 350 mb, 500 to 600 mb, and from 800 to 925 mb. Although 2300 GMT NSSL rawinds and the 0000 GMT NWS rawinds were used for editing of both wind sets, care was taken in their application to the 2120 GMT wind set due to the time difference. Only for the 2314 GMT wind set were the rawinds added directly into the analysis. For this reason the 2314 wind set coverage is more complete and is the one illustrated in the following figures. An attempt was also made to add in aircraft winds from the Sabreliner N307D and QueenAire N304D, but biases were found in the wind directions, making them unusable without further refinement.

The final wind sets were analyzed level by level using the Barnes (1973) low pass filter scheme for both hard copy and computer graphics plots. This objective analysis scheme allows a variable filter to reduce noise and small scale variations via the use of harmonic functions. In this way, contoured plots of streamlines, isotachs, horizontal divergence, and vorticity (using a simple centered difference scheme) among others, were produced for various pressure levels and in some cases isentropic surfaces.

Seen in Figures 1a and b, is an example of the vectors (24 rawinds and 88 cloud tracers) for the 2314 GMT 250 mb surface, along with an analyzed field of streamlines and isotachs based on those vectors. The observed pattern is consistent with that seen two hours earlier at 2120 GMT, with a subtropical jet to the south of the severe storm area (such weather was concentrated in the southwest portion of the anvil during this time period) and diffluence in the main anvil area. However, higher velocities in the jet core were observed at 2120 GMT (up to 60 ms^{-1}).

One can see how this pattern generally changed with height by comparing Figure 1 with 2. The latter, a 925 mb plot, shows a pronounced line of confluence approximately where the surface cold front lay. An exception is immediately over the anvil where due to lack of low level vectors, the confluence line is placed too far north. To the south of the front winds are more southerly than at lower pressures: the winds, as one might expect, veer with height. North of the front, a northeast flow is evident.

It is interesting to note that the anvil appears to be moving to the right of the wind at all levels. Evidence of this fact appears in Figure 1b where the western part of the anvil has a west-east orientation instead of the expected southwest-northeast one. The vectors along the anvil edge show the same deviation. This rightward motion has been noticed frequently in relation to severe storm behavior (e.g., Newton and Newton, 1975) and more recently in regard to whole anvils (Anderson, 1979). In this case, comparing the vectors at or near both sides of the anvil edge with those in the undisturbed flow upstream, one finds a deviation of as much as 50° from the ambient 250 mb flow (greater deviations occur at lower atmospheric levels). More will be said about this deviation in the subsequent section on small scale cloud features.

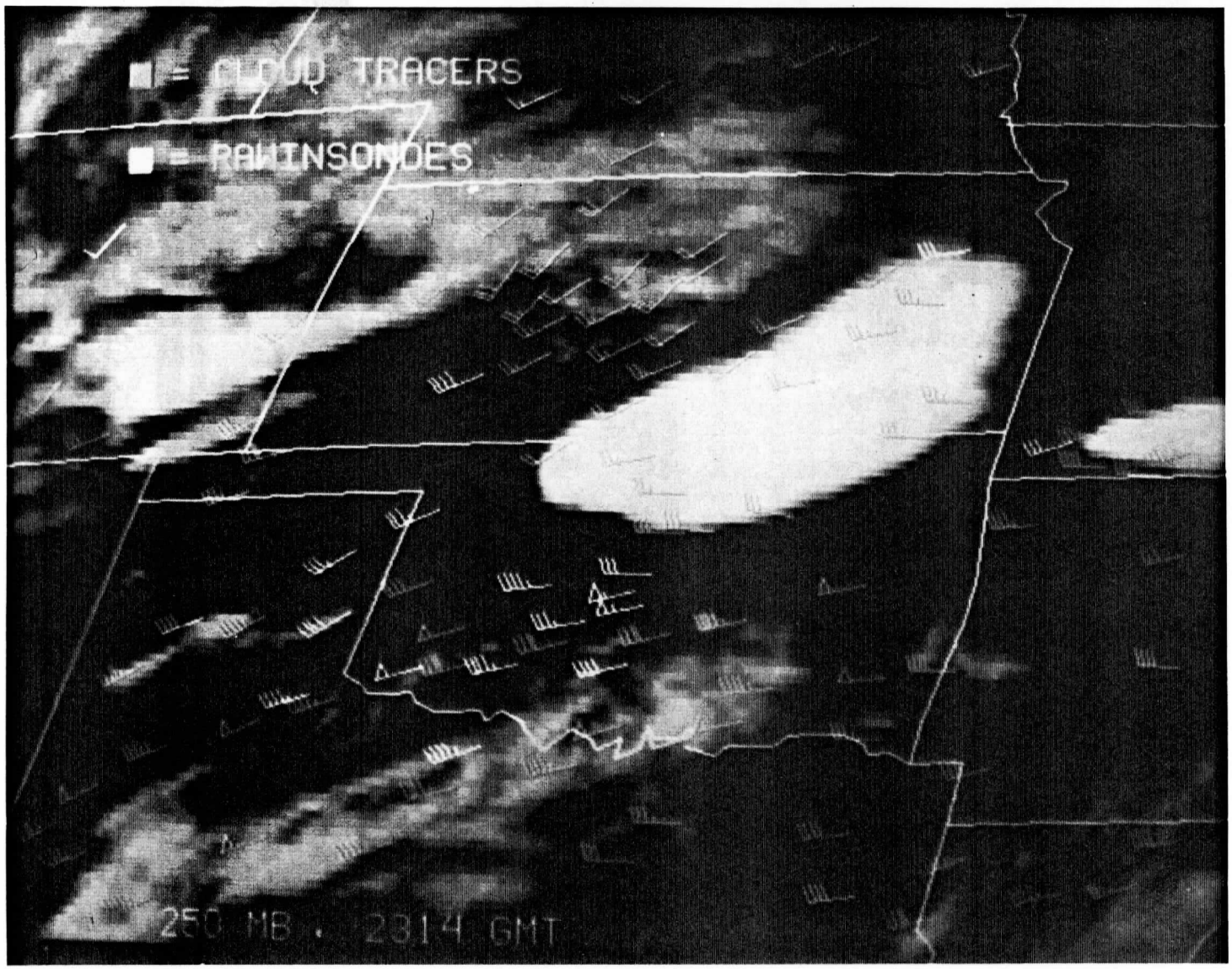

Figure 1a. May 2, 1979, 2314 GMT GOES infrared image with transposed 250 mb cloud tracers (light) and rawinds (dark) from 250 mb. Flags are in ms^{-1}.

Figure 1b. Same image as 1a, but with transposed 250 mb streamlines (solid) and isotachs (dashed) in ms^{-1}.

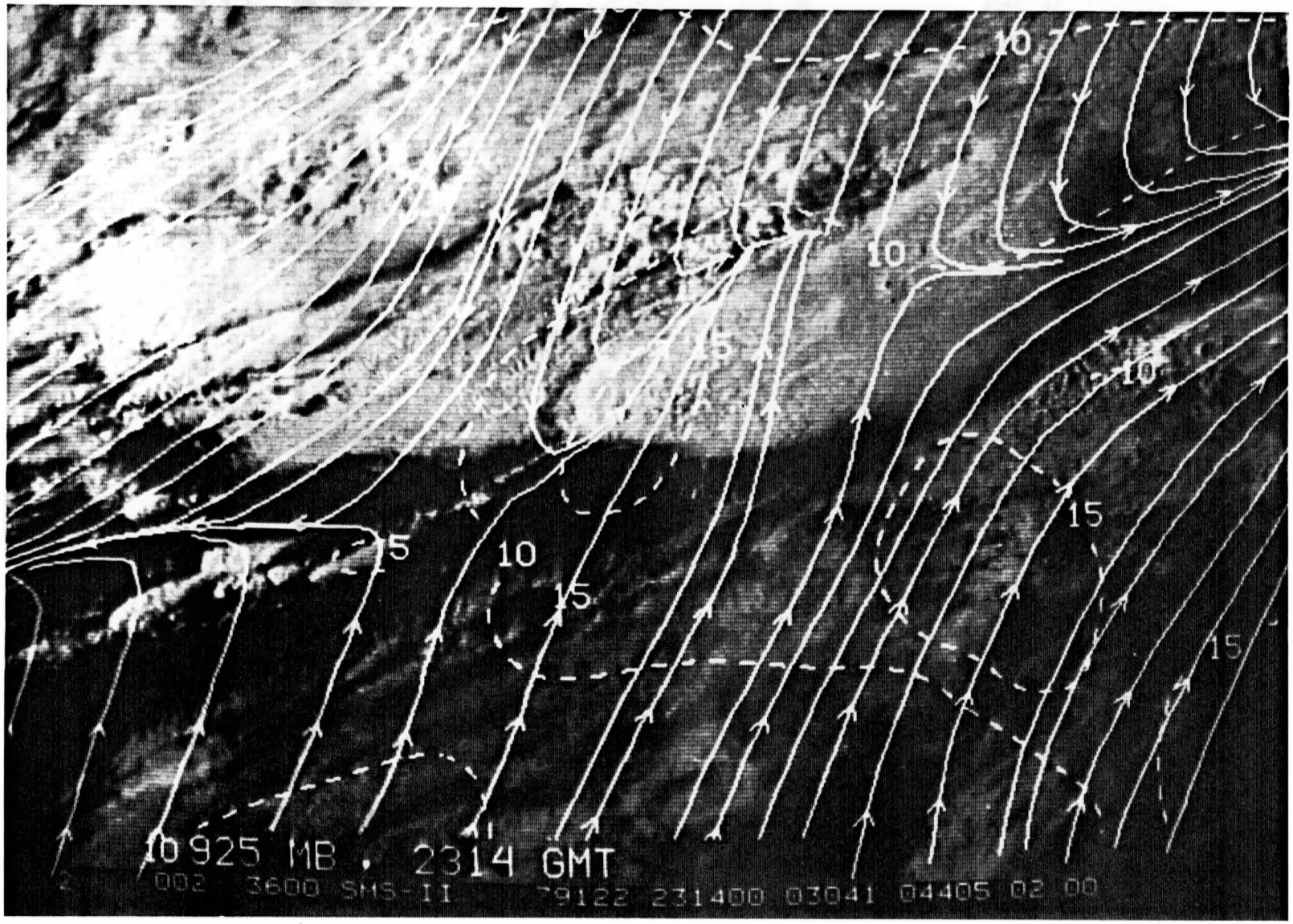

Figure 2. May 2, 1979, 2314 GMT visible image with transposed 925 mb streamlines and isotachs in ms^{-1}.

Looking now at some derived parameters, Figures 3a and b show 2314 GMT horizontal divergence at 250 mb and vorticity and streamlines at 500 mb. The divergence pattern is consistent with that from the earlier wind set, and indicates a band of divergence running close to the front with maximum values in excess of 15 x $10^{-1}ms^{-1}$ over the anvil. Convergence can be seen both north and south of this band. The 500 mb streamlines show a small positive vorticity center over the southwest portion of the anvil associated with a weakening short wave (described by Bluestein et al., 1980) and another positive area in association with a clump of smaller storms further to the west. The data was, however, rather sparse in that area.

Figure 4 shows the divergence and vorticity at low levels. Two divergent centers of about 1 x $10^{-4}s^{-1}$ are to be found slightly to the west of the two centers of convective activity within the anvil. At low levels, an area of cyclonic vorticity right over the severe storm area can be seen. Upper level vorticity (not shown) is also cyclonic but weaker (about 1 x $10^{-4}s^{-1}$).

Finally, Figure 5 shows two 288° isentropic surface analyses: the first with streamlines and pressures, the second with moisture divergence. The first plot is interesting in that it suggests significant upward motions at low levels over the western part of the anvil, especially near the severe storm area where the streamlines become more perpendicular to the pressure gradient. Upward motion is also indicated to the south of the front, although it is relatively weak and of doubtful significance given the strong convergence found to the south of the storm at upper levels (Fig. 3a) and the weak but general divergence at low levels (Fig. 4a). To

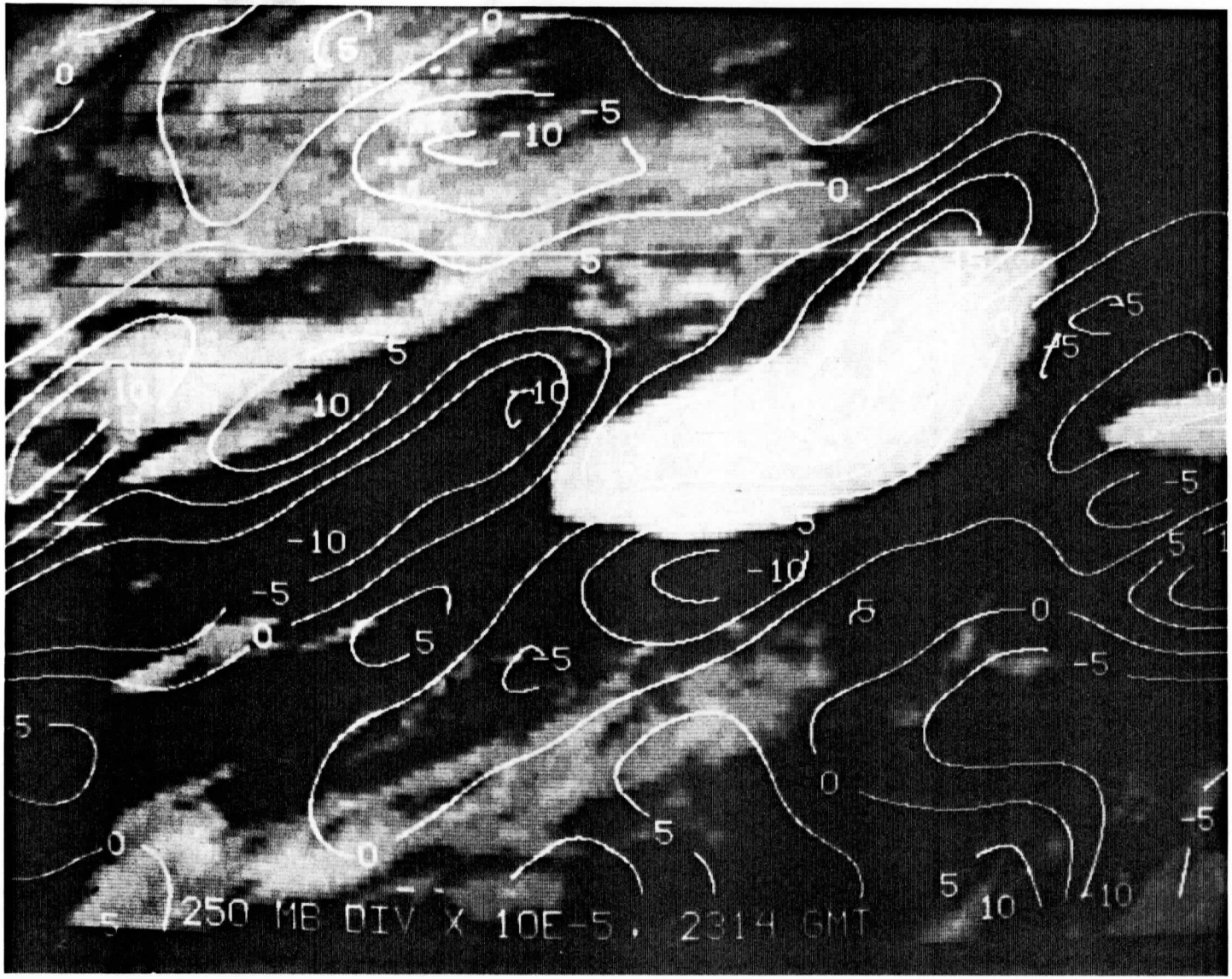

Figure 3a. May 2, 1979, 2314 GMT infrared image with transposed contours of 250 mb horizontal divergence (x 10^{-5} s^{-1}).

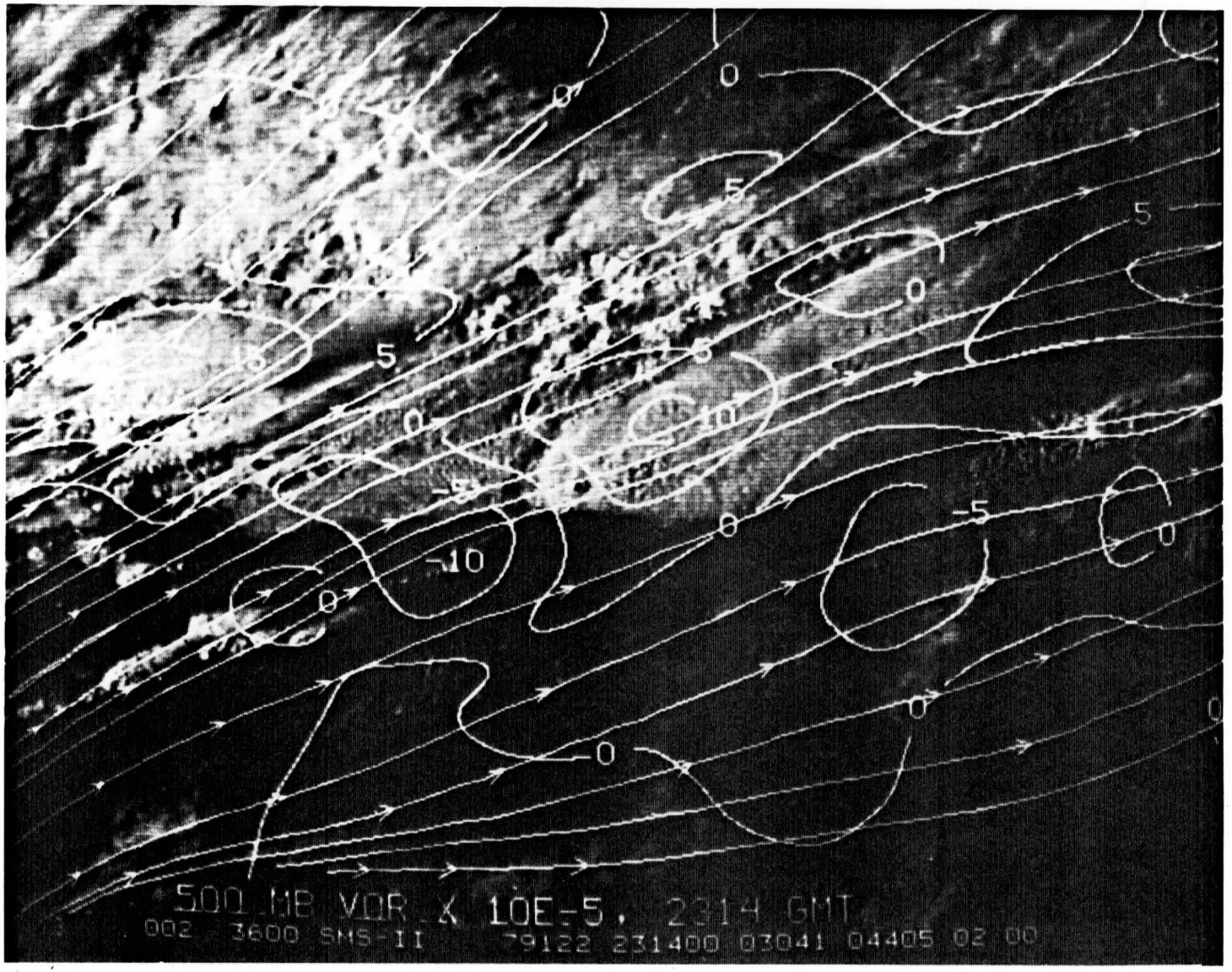

Figure 3b. 2314 GMT visible image with 500 mb streamlines and contours of vorticity (x 10^{-5} s^{-1}).

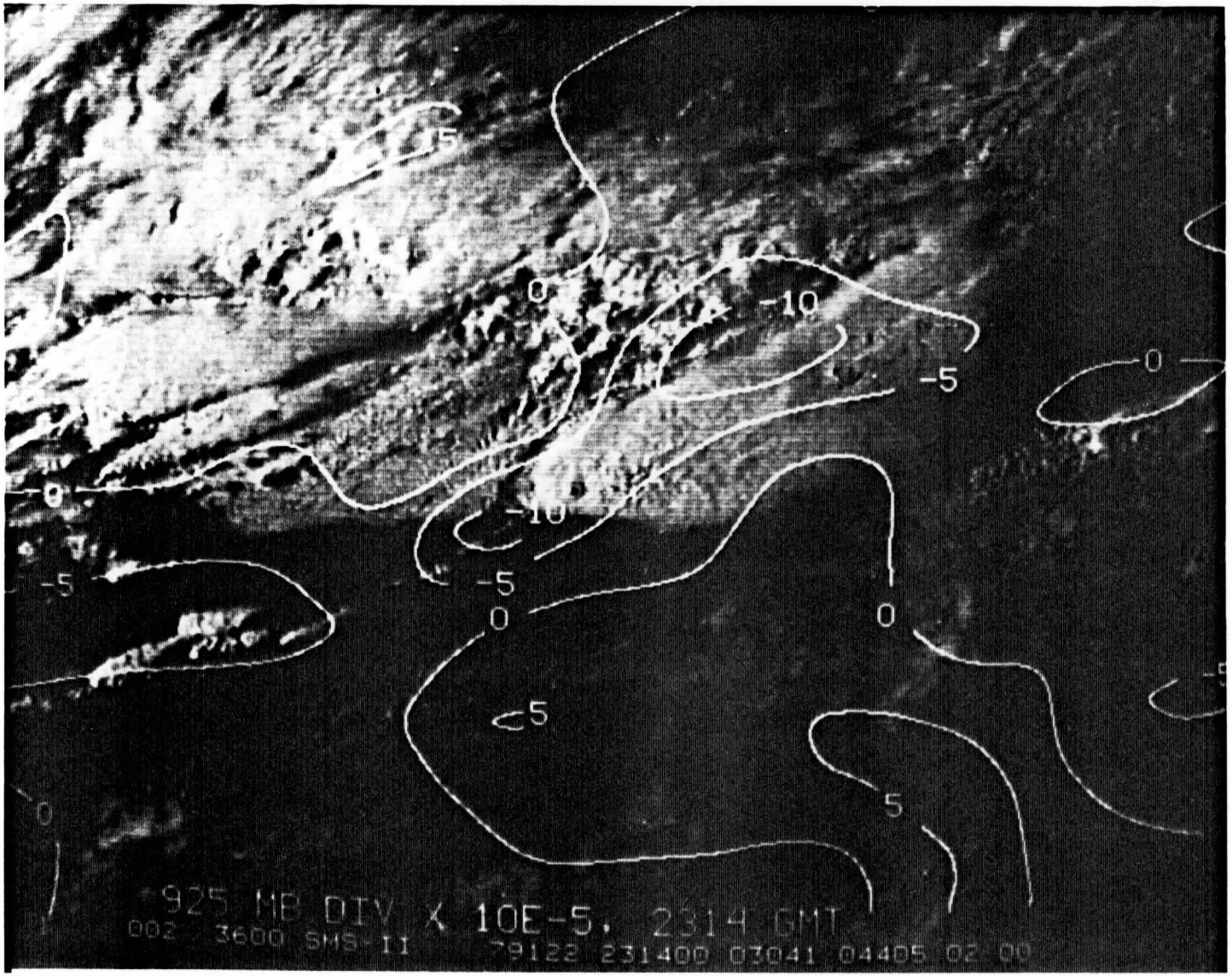

Figure 4a. May 2, 1979, 2314 GMT visible image with contours of 925 mb divergence.

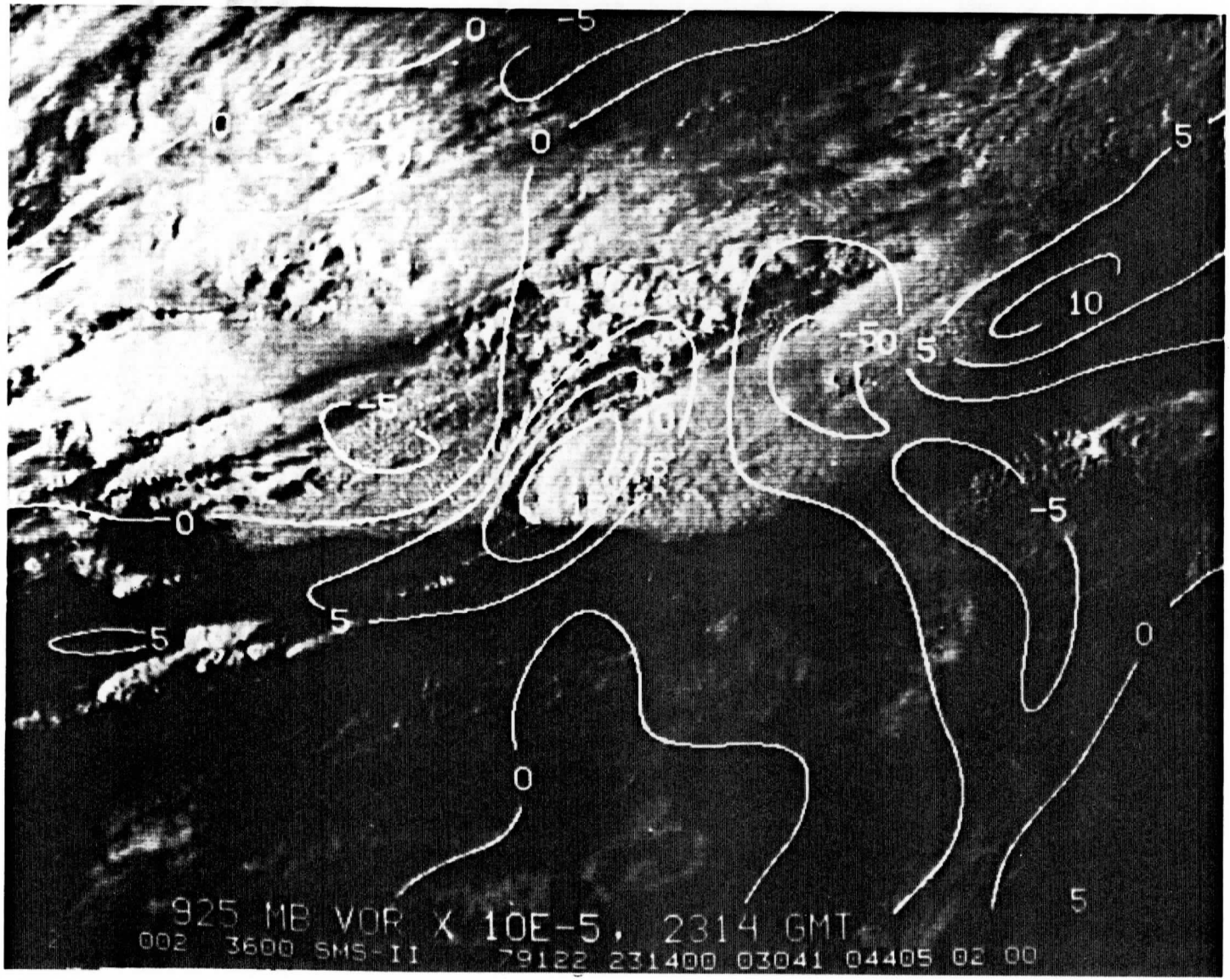

Figure 4b. Same as 4a, but with contours of vorticity.

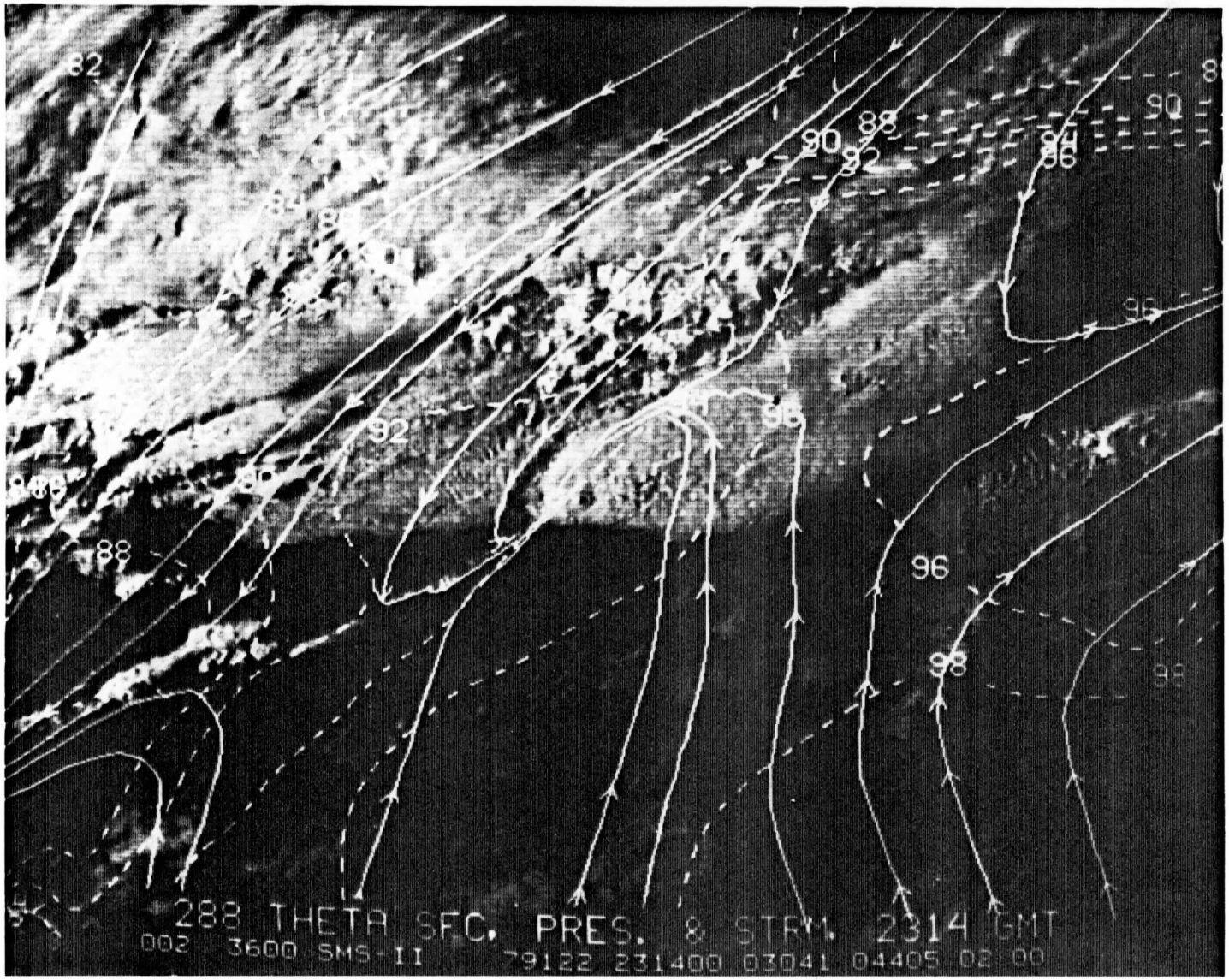

Figure 5a. May 2, 1979, 2314 GMT visible image with contours of pressure (mb x 10^{-1}) (dashed) and streamlines (solid) on a 288° theta surface.

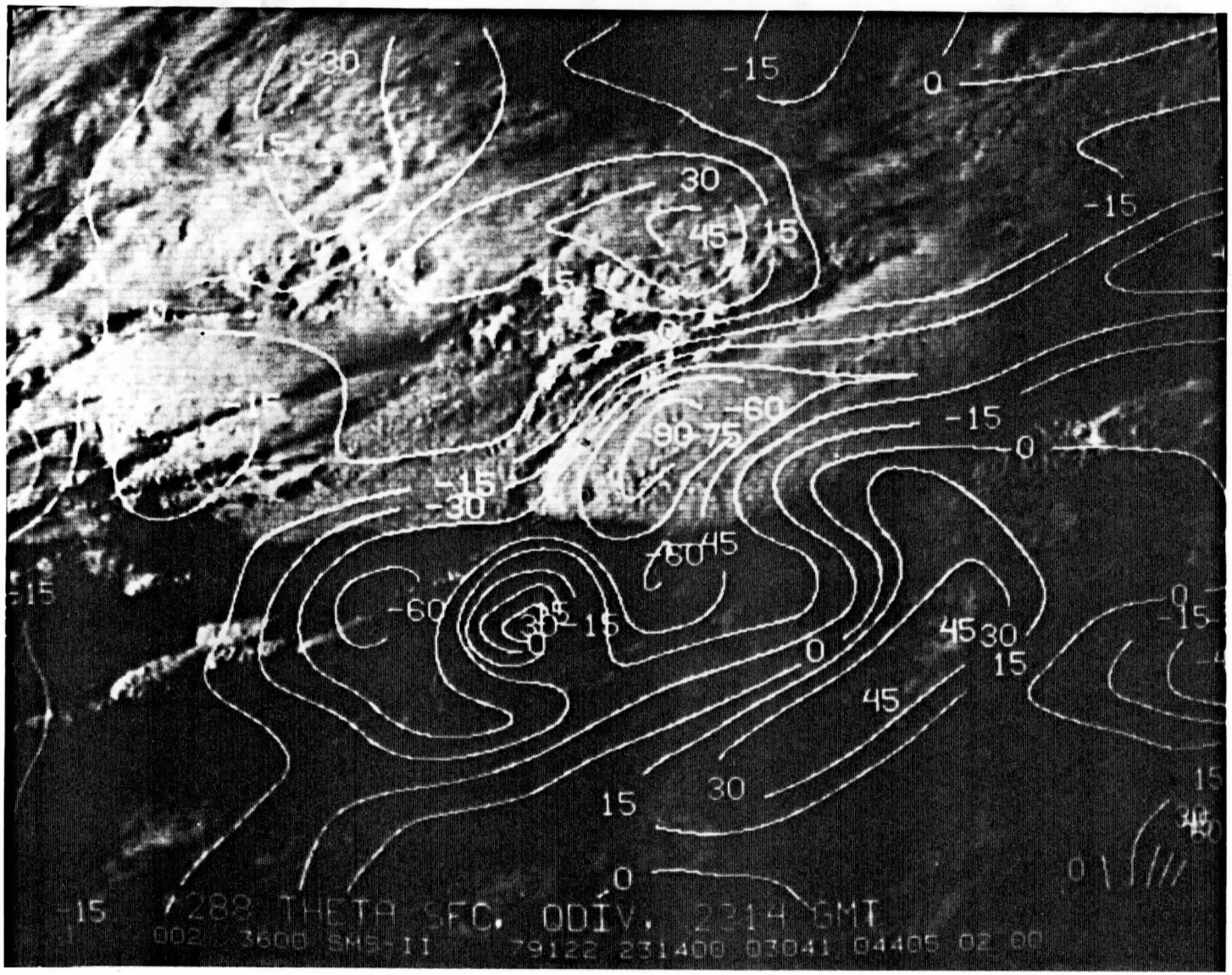

Figure 5b. Same as 5a, but for moisture divergence (gkg^{-1} s^{-1}) instead of pressure and streamlines.

the north of the front, motions are downward except in association with an area of clouds to the north-northwest.

Moisture convergence, as an important condition for severe storm development, has been given recent attention by Negri and Vonder Haar (1980). Calculated from $\nabla \cdot qV$, favorable moisture convergence is found in the anvil area and to a lesser extent, along the whole frontal boundary.

In summary, the environmental wind field has illustrated, in a number of respects, that conditions existing in the severe storm area were propitious to the maintenance and intensification of convection. These include favorable vertical shear, including the veering of the winds with height and evident propagation of the storm cells into the warm moist air to the south; the movement of a frontal boundary into the area of interest; upper level divergence, and low level convergence over the storms; the presence of a 500 mb short wave over Oklahoma; and the indications at low levels (the 288° theta surface) of substantial upward motion and moisture convergence.

While the results are not particularly unusual for a severe storm environment, they are based on data having higher vertical and horizontal resolutions than the usual conventional analyses, and thus allow one a greater certainty about what is happening at the actual storm site. This advantage would be particularly useful for performing future quantitative studies of mass and moisture budgeting in the vicinity of the storm. In addition, small scale phenomena in which there has been recent interest, such as gravity waves and outflow boundaries, can be measured and tracked with the help of such data.

While the usefulness of cloud tracer motions integrated with conventional data is significant, one must keep in mind some of the

practical considerations that went into an effort such as the one presented here. Obtaining a good research-quality (as opposed to operational) tracer set is dependent on the ability to track clouds accurately and assign them to the proper heights. For example, tracking each of these wind sets took approximately 20 to 30 hours of McIDAS time and an additional 20 to 30 hours of time to do editing, height assignment and integration with conventional data. Even though we would have liked to do an additional wind set prior to the formation of deep convection, our resources were already stretched too thin with our first two wind sets. Although far from precluding the use of cloud tracers in the manner just described, the time and expense involved in wind tracking puts some practical limitations on the extents of the analysis.

4. Small Scale Storm Features

In this section we will deal with that part of the study investigating satellite-observed small-scale cloud features and their relation to severe weather events. Previous work in this area has concerned itself mainly with cloud top heights and their variation over time. Shenk (1974) using aircraft, and Suchman and Krause (1979) using satellite have successfully linked overshooting tops with the presence of severe weather. In some cases, investigators (Pearl, 1974; Umenhofer, 1975; and Fujita, 1972) have suggested that a leveling off or a decrease in cloud top heights precedes a tornado touchdown. Using satellite infrared with a coarser resolution, Adler and Fenn (1979) find an interval of cloud top ascent just before a touchdown.

We have attempted to look at anvil detail from a different point of view; namely, that of following the horizontal motions of the anvil detail

and relating this movement to the environment, especially severe weather events. To accomplish this task, we have used three sources of data: full resolution visible (1 km) and infrared (4 km) GOES satellite data for May 2, 1979 at three minute intervals; NSSL WSR-57 CAPPI radar data from Norman, Oklahoma; and surface severe weather reports as compiled in Alberty et al. (1979).

A particular focus of our effort was the study of overshooting tops, readily apparent in the visible satellite data shortly after the formation of the anvil associated with severe weather (1930 GMT) and continuing on until visible data was no longer available (0000 GMT, May 3). These tops, while rapidly changing, appeared to be trackable using the same techniques for tracking clouds that were described in the last section. We hoped such features might provide some insight into events taking place beneath the anvil itself.

The actual tracking of anvil features proved difficult. Even with three-minute data, continuity of the cloud features over time was hard to establish. Confusion was also compounded by the low sun angle during the period of study. Long shadows cast by the tops changed rapidly and unpredictably. Finally, one kilometer resolution data is marginal in its ability to distinguish features on this scale. One cannot actually see individual towers; rather, one sees areas of high tops which have some continuity but also a highly changeable geometry.

Even with these obstacles, we found it possible to track some anvil features using unaltered imagery like that shown in Figure 6a. However, trackable detail was much increased by applying a high pass filter to the digital satellite data (Figure 6b). This filter had the effect of enhancing small scale features within the anvil in relation to their

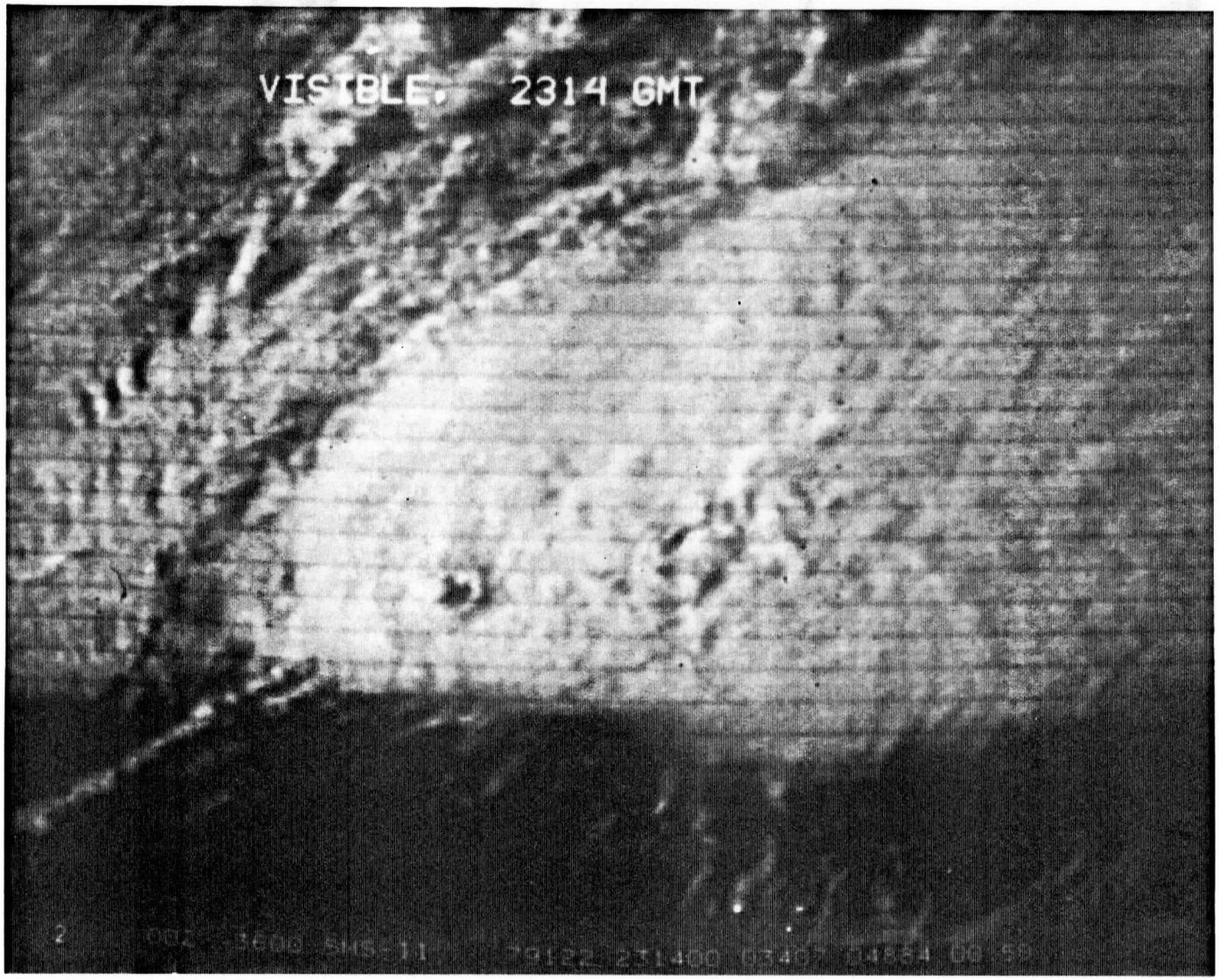

Figure 6a. Eight times blowup of the May 2, 1979 severe weather area at 2314 GMT.

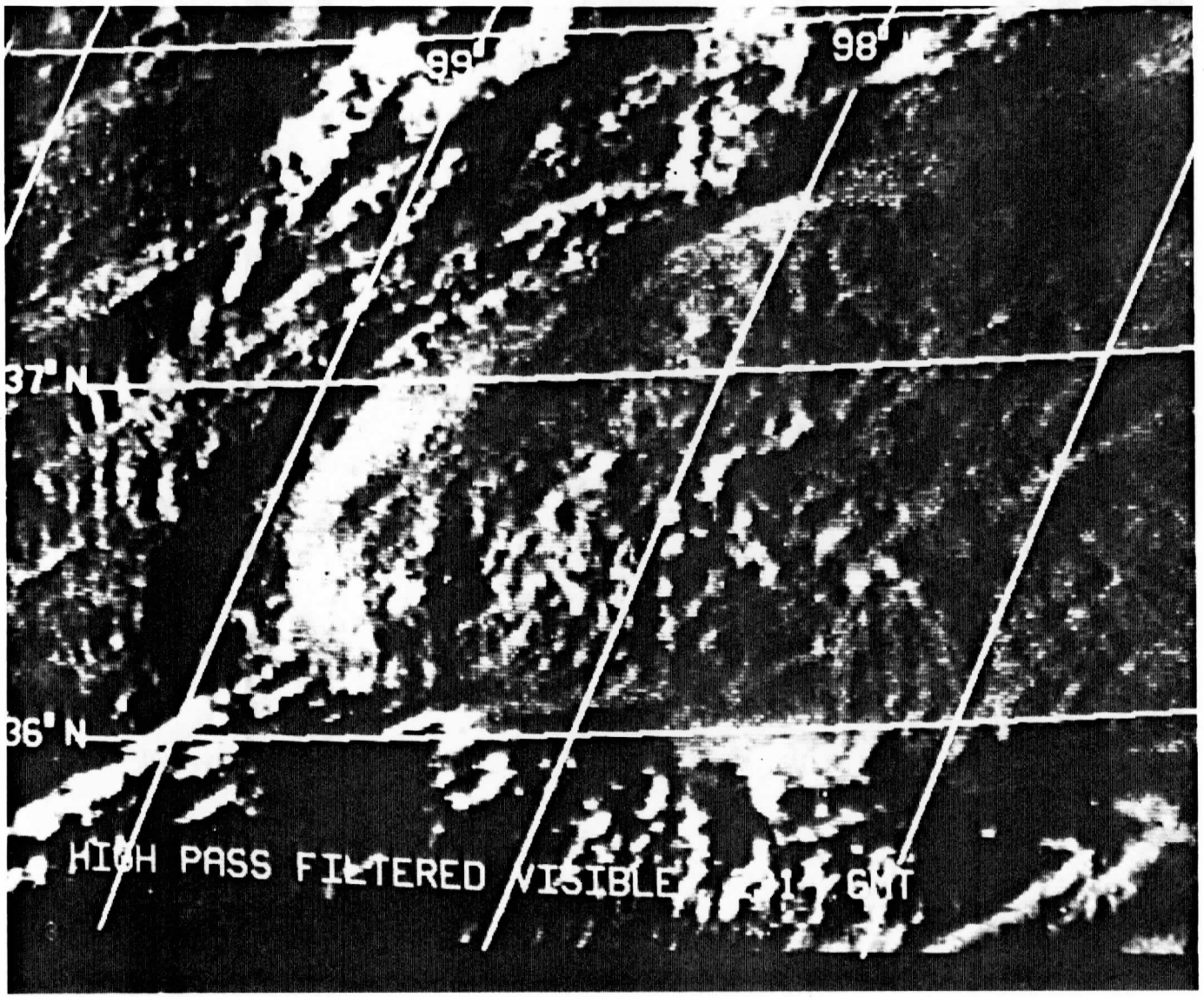

Figure 6b. Same as 6a, but with brightnesses subjected to a high pass filter.

background. Using this filter on satellite imagery from 2300 to 2330 GMT, we were able to obtain three anvil motion sets based on sequences of three images spaced at three-minute intervals. These anvil motion sets were centered on 2311, 2317, and 2323 GMT. As in the wind sets of the last section, we used single point tracking. Attention was confined to the western half of the anvil. There were additional overshooting tops from an active convective center in the eastern half of the anvil, but this area was not associated with significant severe weather during the period of analysis.

The results for the anvil motion study can be seen in Figure 7. Vectors, a total of 50 per set, were produced over an area covering the western half of the anvil, but not all of them were from overshooting tops. There appear to be more diffuse features inside the anvil which resemble bands or streamers. Although these have a consistent motion, they appear larger and more diffuse, lacking the shadowy highlights of the cloud tops. These features can be seen in Figure 6b along the edges and in the eastern part of the anvil. Their behavior differed from the overshooting tops in that they tended to move faster and appeared to diverge away from the anvil centerline. Thus, while the tops moved from the west at about 10-25 ms^{-1} (average = 18 ms^{-1}), the non-tops usually had a northeasterly or southeasterly movement at speeds of 15 to 45 ms^{-1} (average = 28 ms^{-1}). We are not certain of the exact nature of these features, although gravity waves, patterns of air circulation within the anvil (Anderson, 1982a), and stratospheric cirrus (Fujita, 1982) are all possibilities.

It is tempting to treat the anvil motion vectors like any other winds and attempt to derive some kinematic quantities such as divergence and vorticity from them. Recently, Anderson (1982b) has attempted to do just

that, using anvil motions from another storm. There are a number of reasons why this would seem ill advised in this case study. First, as already pointed out, the anvil motions are based on two seemingly different kinds of tracers. At a minimum, it would be necessary to distinguish clearly between these tracers (not always an easy thing to do) and perform separate analyses on them. More important, the accuracy with which these anvil motion were tracked was limited by the problems described earlier. While the general range of speeds and directions inside the anvil have been measured as accurately as possible, the tracer set would not provide meaningful results if second order differences were being calculated. This area of investigation was therefore not attempted.

For purposes of comparison, the tornado tracks (labeled T_1, T_2, T_3) for the period 2215 to 2355 GMT have been included along with anvil motion tracks (unlabeled) in Figure 7. One can see that both the tops and the

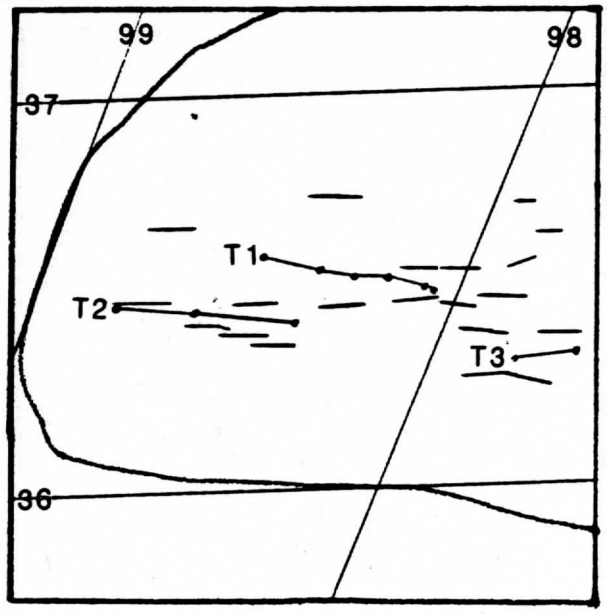

Fig. 7. May 2, 1979, 2311 GMT anvil motion tracks and the tracks of three tornadoes in existence over a two-hour period, labeled T_1 (2215 to 2320 GMT), T_2 (2217 to 2250 GMT), and T_3 (2345 to 2355 GMT). The heavy outline is the anvil boundary.

tornado tracks shared a similar direction of motion. In addition, the tornadoes moved at speeds ranging from 10 to 22 ms^{-1} toward the east, about the same range of speed as the cloud tops (10 to 25 ms^{-1}). Thus the tops and the surface severe weather appear to be traveling together. One may remember from the preceding section that these anvil motions also deviate to the right of the environmental winds at all levels and are similar to the overall motion of the anvil.

The Norman WSR-57 radar echoes from 2244 to 2330 GMT associated with this anvil were also tracked using the same techniques. The spacing between the radar images was variable, usually 3 minutes, but as much as 9 minutes in one case. Finding detail distinguishable over time was difficult and there were relatively few echoes; however, the echoes that were present were large and stable. Using 6 loops of 3 images each resulted in sets of vectors with several tracers from each echo.

A similar correspondence in motion between the radar echo and the tornadoes was also measured. The echoes had speeds ranging from 13 to 30 ms^{-1} moving due east on the average.

Another characteristic of the cloud top motion, not apparent from Figure 7 but illustrated in the next section, is the grouping of cloud tops into clusters. The tops do not exist as isolated peaks, but appear to be associated with other bright tops in the visible images. Although it is difficult to follow an individual top over time, the cluster of peaks in which it is embedded has good time and size continuity. Thus, while it is difficult to say whether a tornado is associated with a particular peak, such phenomena have a clear connection with a particular group of cloud tops.

Variations with time of the anvil motions were difficult to extract over the short 30-minute time span studied, but speeds of the tops tended to increase over the period. Also, speeds were slower in the western part of the anvil than they were in the east. This may be due all or in part to the greater number of non-tops tracked in the east.

In summary, the motions of the overshooting tops close to the site of the severe weather appear to be related more to the speeds and directions of tornado and radar echo movement than to the environmental flow at upper levels. These tops also appear to organize into groups or clusters which have continuity over time and may be more useful than the individual tops themselves (which are rapidly changing) in monitoring storm activity. In addition to the tops, there are other features identifiable in the visible images that appear to have a different morphology. These "non-tops" generally move at a direction and speed at variance with the tops, but their physical nature and origin is not certain. As these results are based on only one case study, it is an open question whether such results have general validity.

In evaluating the usefulness of this type of analysis, one should first consider future research possibilities: There remain some interesting questions to be answered about the character of anvil motions. We have raised one such question already in stating the need to generalize the results presented above. Another major problem has to do with the morphology of the tops themselves. What is it that we are looking at in the satellite view? In addition to the distinction between the tops and non-tops mentioned earlier, there are difficulties in describing the overshooting tops themselves. Are there really "holes" in the anvil as described by Anderson (1982b)? More generally, what is the morphology of

the tops and how does this morphology translate into what we see in visible and infrared satellite imagery? These questions might be most directly resolved by doing simultaneous aircraft and satellite studies of the same storm. Yet there are other less intensive methods of research on anvil features which could take advantage of the same data as we have used here. One potential area of endeavor would be to examine the behavior of the overshooting tops in more detail over time. If cloud tops do occur in clusters, how does the cluster change over time, both in regard to average brightness, areal extent, and speed of motion? The use of stereoscopic techniques such as those described in Hasler (1982) would be useful in quantifying the height variations of the cloud tops over time within the cluster. Do these variables show a relation to the life cycle of storm cells (including precipitation extent and intensity, occurrence of severe weather, anvil expansion, etc.)? How do cloud tops behave in less severe storms? Would any of these results lend themselves to providing storm intensity indices?

These questions indicate that there is a great deal of potentially useful information yet to be excavated in the area of anvil mesoscale characteristics. What makes this area of research more attractive is that the information on anvil motions is relatively easy to extract. Admittedly, tracking features within the anvil is difficult and must be done carefully. This is more than balanced by the fact that the area to be covered is relatively small and the task of assigning cloud heights is less time consuming since most of the tops are around the same level. In comparison with the cloud drift winds of the previous section, the anvil wind sets were done in about half the time. Further investigations in this area are highly recommended.

5. Severe Weather - Satellite Digital Brightness Relationships

One of the three main goals of this project as stated in the proposal was to "improve means whereby satellite brightness data can be used both to isolate deep convection and to detect severe weather in its incipient stages." More specifically, this section deals with the statistical relationship of satellite brightness to radar and surface weather, and the location of severe weather relative to satellite brightness patterns and its change with time.

The data used includes three-minute rapid-scan GOES visible and IR images for May 2 and May 20, 1979, and WSR-57 radar stationed at Norman, OK. The radar, with a 2° beam width, a 1 km gate, and a 200 km range (Fig. 8a), was remapped into the satellite projection for an accurate overlay. An example of this can be seen in Fig. 8b. The remapped radar echoes were then tracked; the speeds as well as the directions were similar to those found for the anvil tops (see Section 4).

The satellite brightness data could also be compared with that of the remapped radar. Two and three channel histograms are used to illustrate this relationship. Fig. 9 shows a three-dimensional histogram of 1000 m radar vs. infrared temperature at 1938 GMT on May 20, 1979, corresponding to a time when the storms were in a developing stage. Two distinct peaks are evident: one at relatively warm temperatures and low reflectivities, indicating the possibility of light showers; a second, stronger peak, is found with relatively cold infrared temperatures and low radar reflectivities. This indicates an abundance of non-precipitating high (anvil cirrus) clouds.

A similar plot for 2314 GMT is seen in Fig. 10. During the elapsed time, we see a marked increase in the cold infrared/high reflectivity

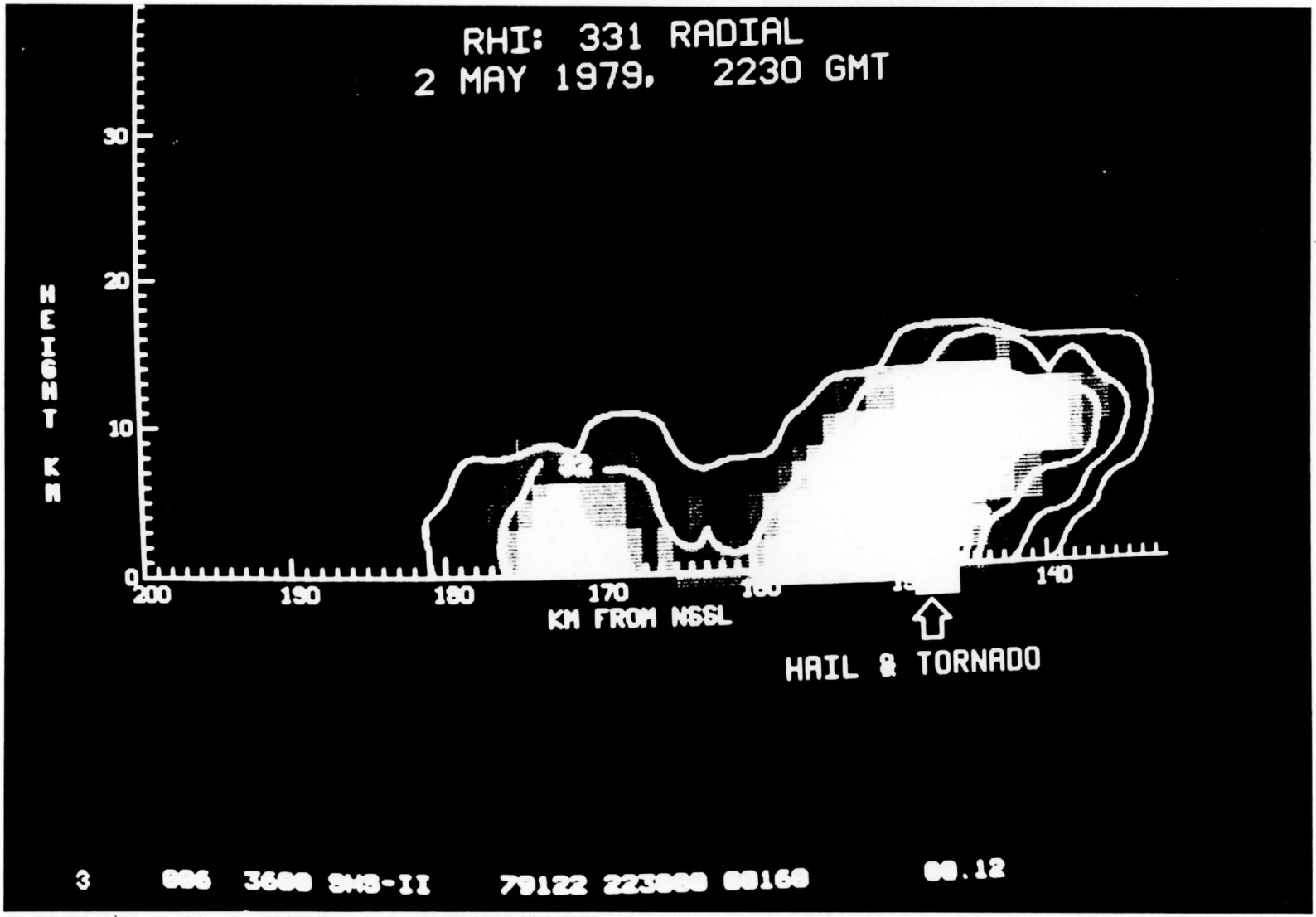

Figure 8a. RHI plot, May 2, 1979, 2230 GMT, centered at NSSL.

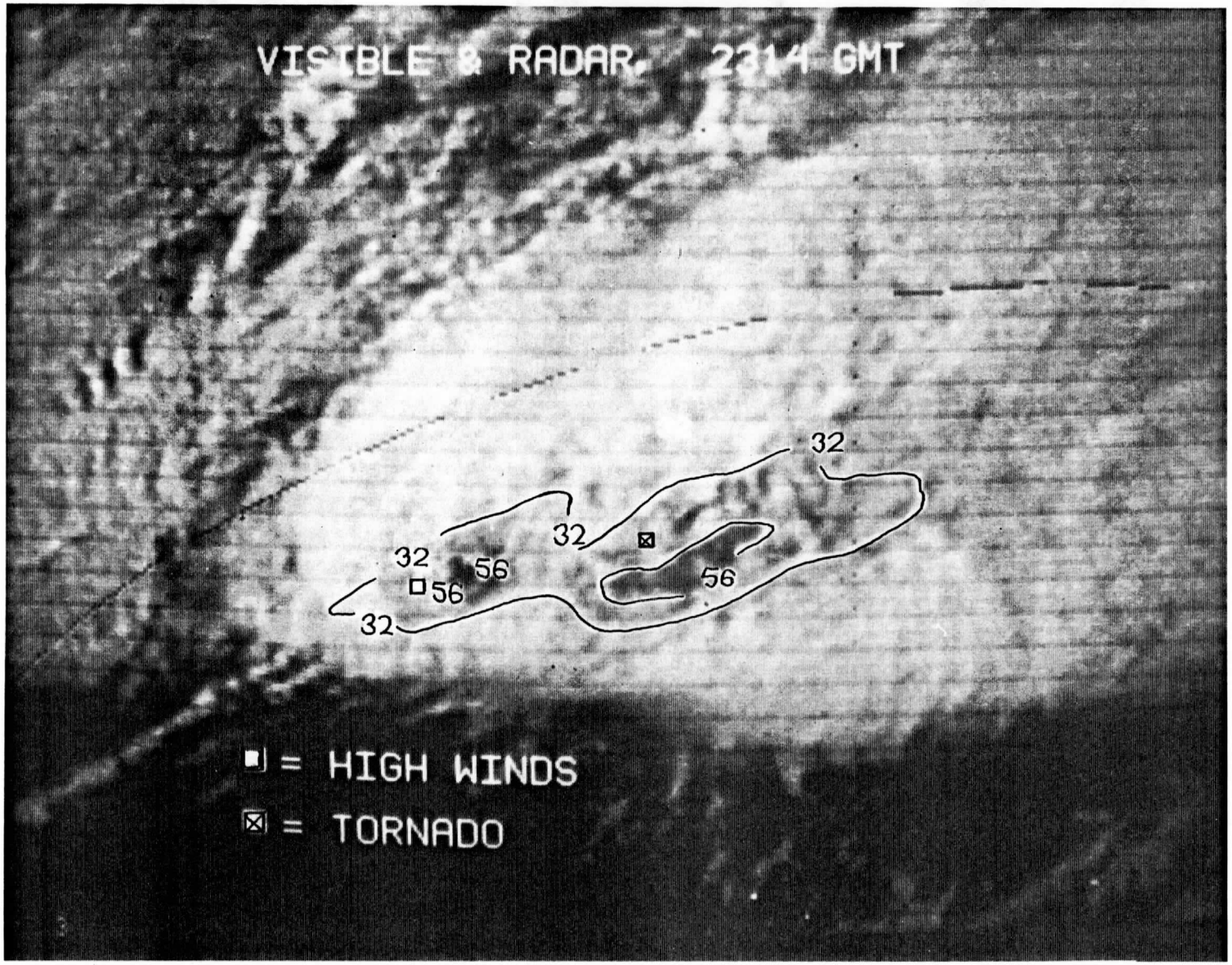

Figure 8b. Full resolution GOES visible image, May 2, 1979, 2314 GMT, with radar overlaid.

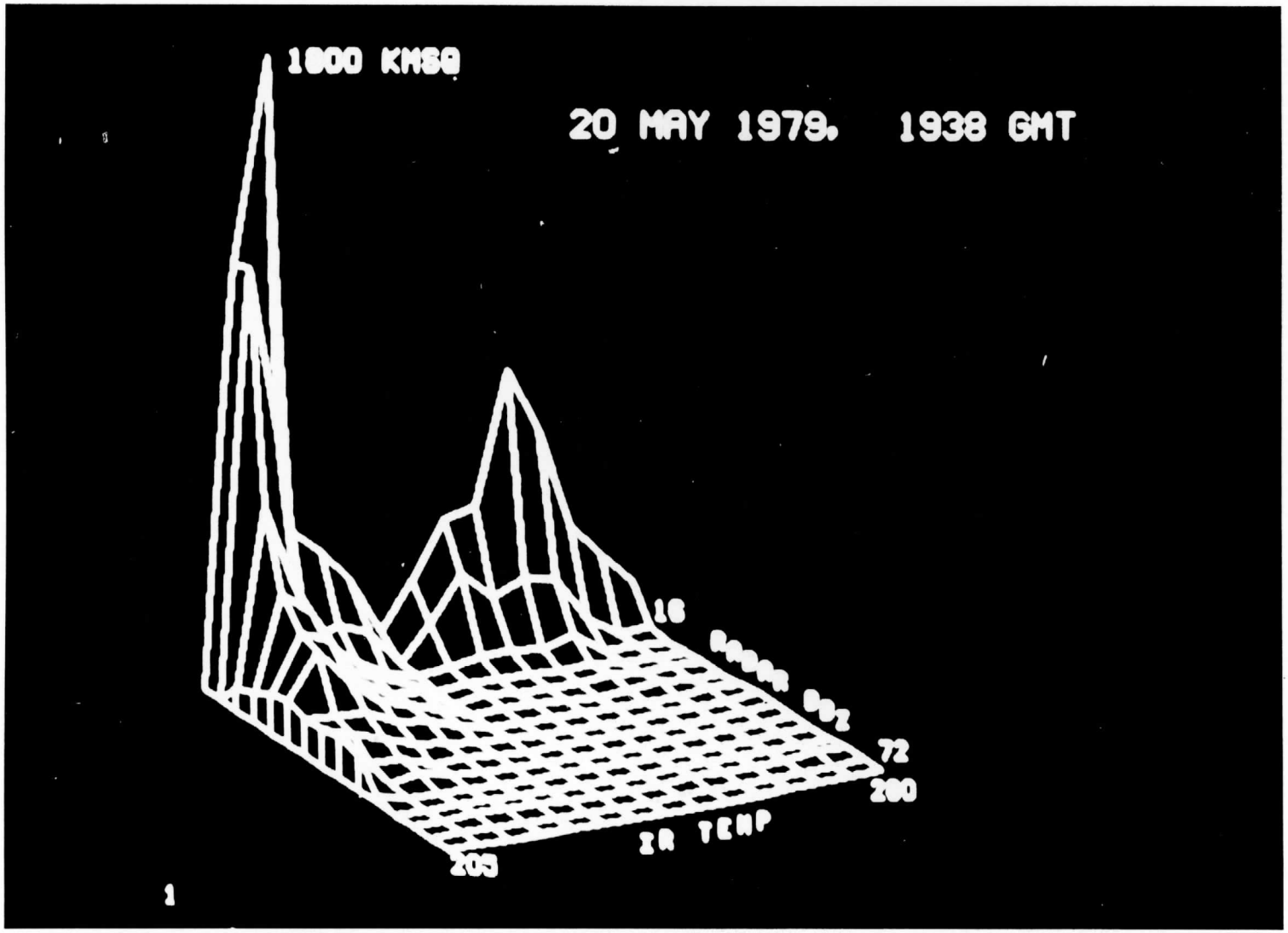

Figure 9. Three-dimensional histogram of 1000 m WSR-57 radar (Norman, OK) vs. GOES 4 km infrared temperatures (°K). 1938 GMT, May 20, 1979.

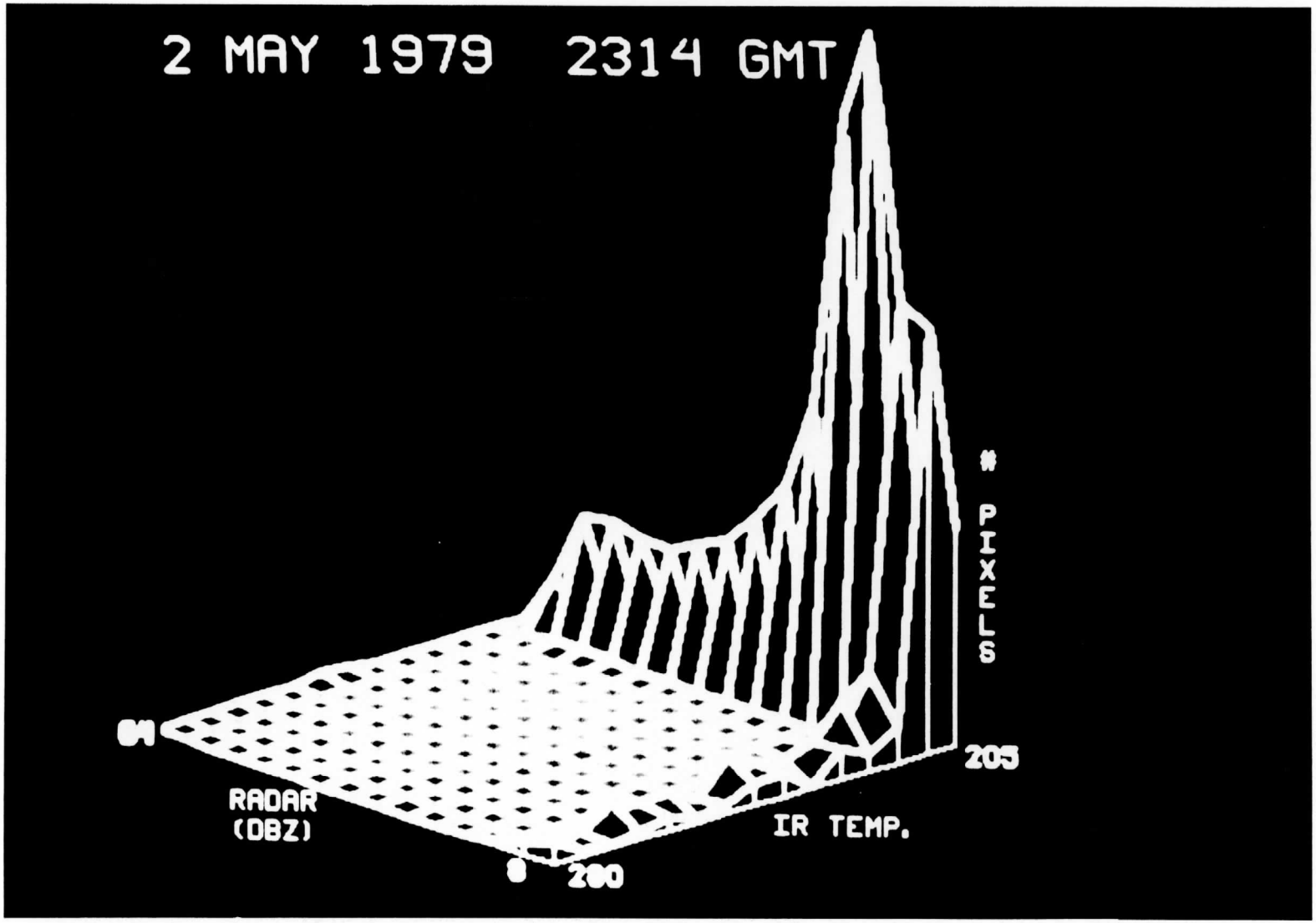

Figure 10. Same as Fig. 9, except 2314 GMT, May 20, 1979.

domain, indicating an increase in system development with precipitating clouds having high tops.

This process can also be expanded to three channels. Channels one and two would correspond to visible and infrared digital satellite data, and the third channel would correspond to radar reflectivities. In this way, clouds that are high (high IR), deep (high vis) and raining heavily (high radar), indicative of well developed thunderstorms, can be isolated. These histograms provide a way of statistically illustrating the domains of shallow versus deep convection, precipitating versus non-precipitating clouds, and light versus heavy rainfall.

The task of relating surface weather to features observed in satellite images is not a new one. For example, Hasler (1981) has shown the proximity of tornadoes to the highest observed cloud tops, while Adler and Fenn (1979) have found tornadoes in the sharp gradient region of cold infrared cloud temperatures.

Our approach has been to construct detailed brightness contour maps of cloud tops using either the visible (Fig. 11) or infrared (Fig. 12) satellite channels, or digitized radar. Finally, 24 severe weather reports (for May 2, 1979), including tornado touchdowns, hail, and high winds, were plotted on these images with the surface weather corrected for parallax errors. In over two-thirds of these cases, the severe weather was located near the brightest visible contour (discussed in a previous section) and in the gradient of infrared temperatures defining the cold dome, usually to the northeast of the coldest temperatures (Table 2). Thus, the tornadoes occurred within thick but not necessarily the coldest part of the cloud. This lack of correspondence may be due to the existence of stratospheric

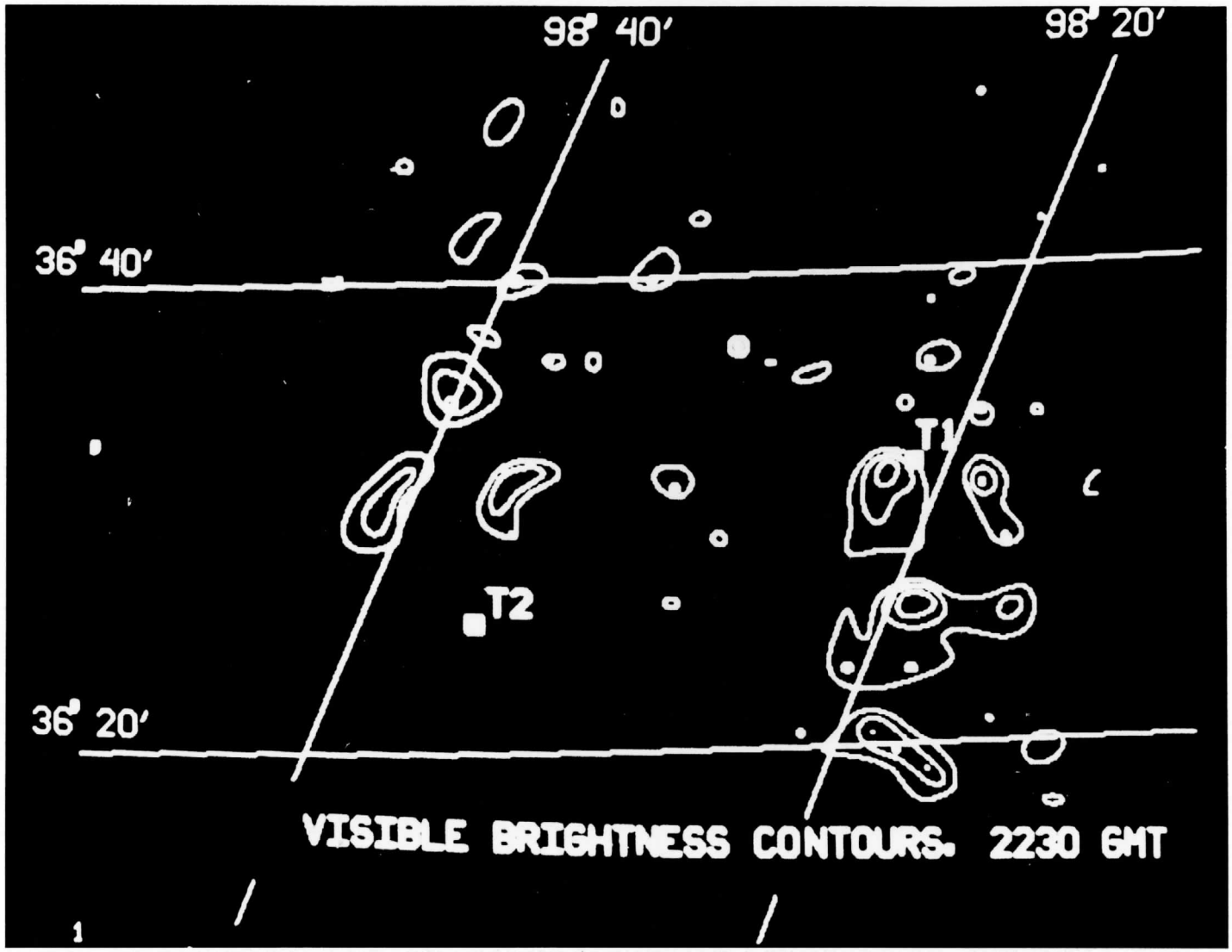

Figure 11. Eight times blowup of visible brightness contours from GOES image, 2230 GMT, May 2, 1979. Contour values range from 180 to 200 digital counts. The locations of two tornadoes, T_1 and T_2, are indicated.

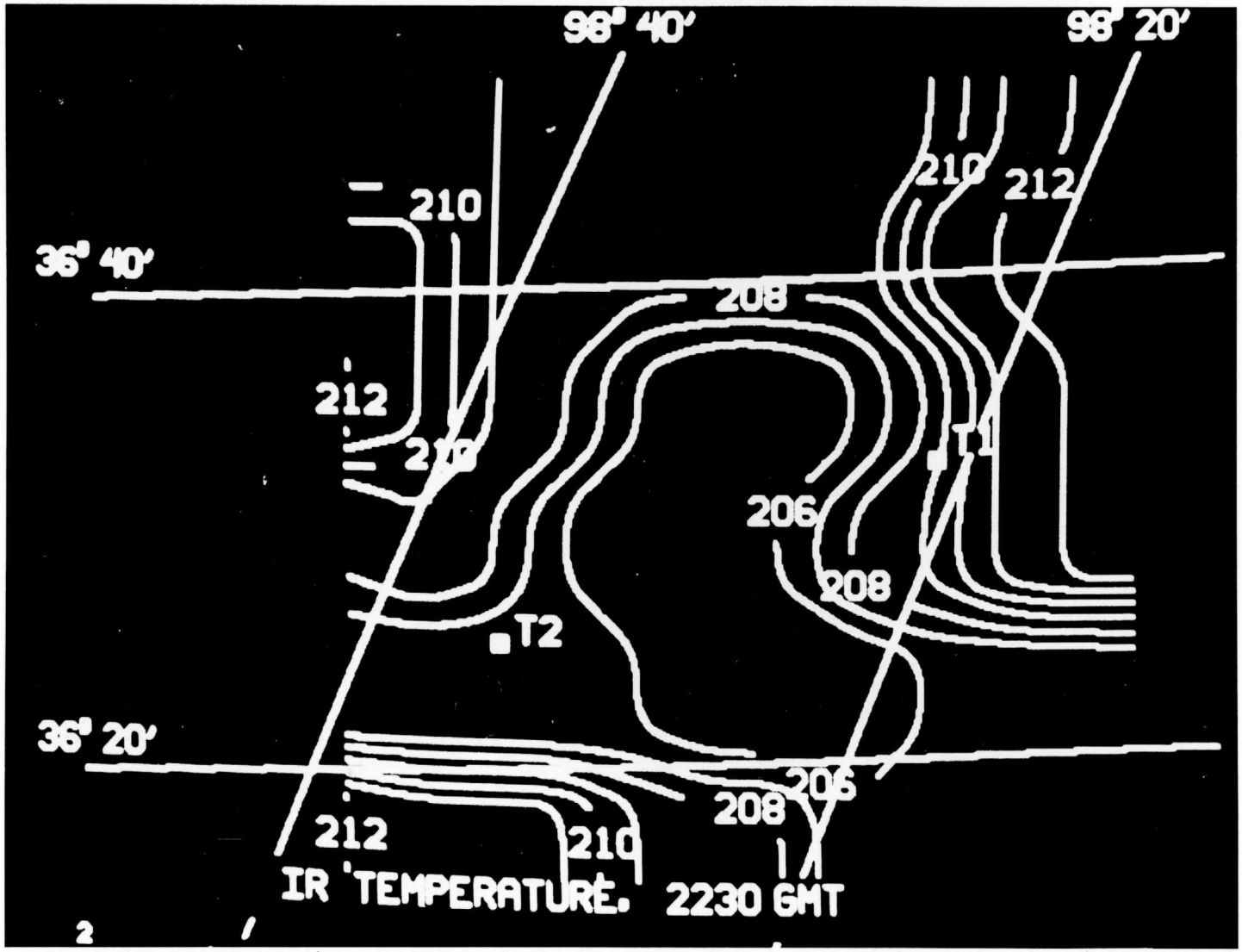

Figure 12. Same as Fig. 11, except for satellite derived infrared temperatures (°K).

Table 2. Severe Weather and its Relation to Satellite Brightness and Radar

Time	Event	Visible	Infrared	Radar
2150	T_1	Near Peak	NE of cold dome in gradient	----
	H_5	Near Peak	NE of warm area, not in grad	----
2000	H_6	Near Peak	NE of cold dome in grad	S of max DBZ
	C_1	Near Peak	E of warm area, not in grad	S edge of echo
2214	T_2	Near Peak	NE of cold dome in grad	S of max DBZ
2217	T_3	Near Peak	S of cold dome in grad	SW edge of echo
2230	T_2	Near Peak	NE of cold dome in grad	S of max DBZ
	T_3	Bright but Flat	In cold dome	S edge of echo
	H_7	Bright but Flat	N of cold dome in grad	S edge of echo
	H_8	Near Peak	NE of cold dome in grad	S of max DBZ
2039	T_2	Near Peak	NE of cold dome in grad	S of DBZ in grad
2250	T_3 (Dis)	Dark Area	Just S of cold max	S edge of echo
2253	T_2	Bright but Flat	Just NE of cold max	S of max DBZ
2300	W_1 and H_{10}	Near Peak	In cold dome	S edge of echo
	H_9	Near Peak	NE of cold dome in grad	S of max DBZ
2314	T_2	Near Peak	NE of cold dome in grad	Near max DBZ
	W_2	Near Peak	W of cold dome in grad	S of max in grad
2320	T_2 (Dis)	Bright but Flat near Dark	N of cold dome in grad	In max DBZ
	H_{11}	Near Peak	NE of cold dome in grad	E of max DBZ
2330	W_3	Near Peak	NE of cold dome in grad	----
	H_{12}	Near Peak	W of cold dome in grad	----
2356	T_4	Transition between bright & dark	E of cold dome in grad	S of max in grad
	H_{13}	Transition between bright & dark	E of cold dome in grad	S of max in grad

cirrus, or to the difference in resolution between the visible and infrared channels.

The relationship of radar and severe weather location is not as well defined. The southern portion of the echoes was often the preferred area for severe weather events, but this proximity varied from virtual coincidence with maximum radar reflectivity to locations along the extreme southern edge of the echo.

In a previous section we noted that tornado velocities were comparable to cloud top speed and direction. While we are not able to say with any confidence that a tornado corresponded to a particular top, we will try to correlate its motion with that of a cluster of tops which can be distinguished from its environment by their relatively high brightness. At 2300 GMT on May 2, 1979, we can see two clusters of tops -- an eastern one, later joined by one to the west (see Fig. 13). Each cluster was associated with its own separate area of high radar reflectivity and each appeared to spawn a tornado which then traveled with the speed and direction of the cluster. T_1, in the subsequent figures, is a vigorous tornado at 2230 GMT, having just widened and intensified. T_2, on the other hand, dissipated at 2250 GMT, 20 minutes after the time shown here. When formed, each tornado was located either under or very near the brightest visible contours, and in the gradient areas of the infrared plots. As time progressed and as the tornado weakened and dissipated, this relationship changed. In the visible, the tornado locations no longer corresponded to the brightest visible or IR gradient region, but now appeared in areas of comparatively flat brightness. T_1 follows this pattern prior to its own dissipation at 2320 GMT. T_1, in Fig. 11, as expected, is near the brightest region while T_2, which is dissipating, is considerably south of this area. In the

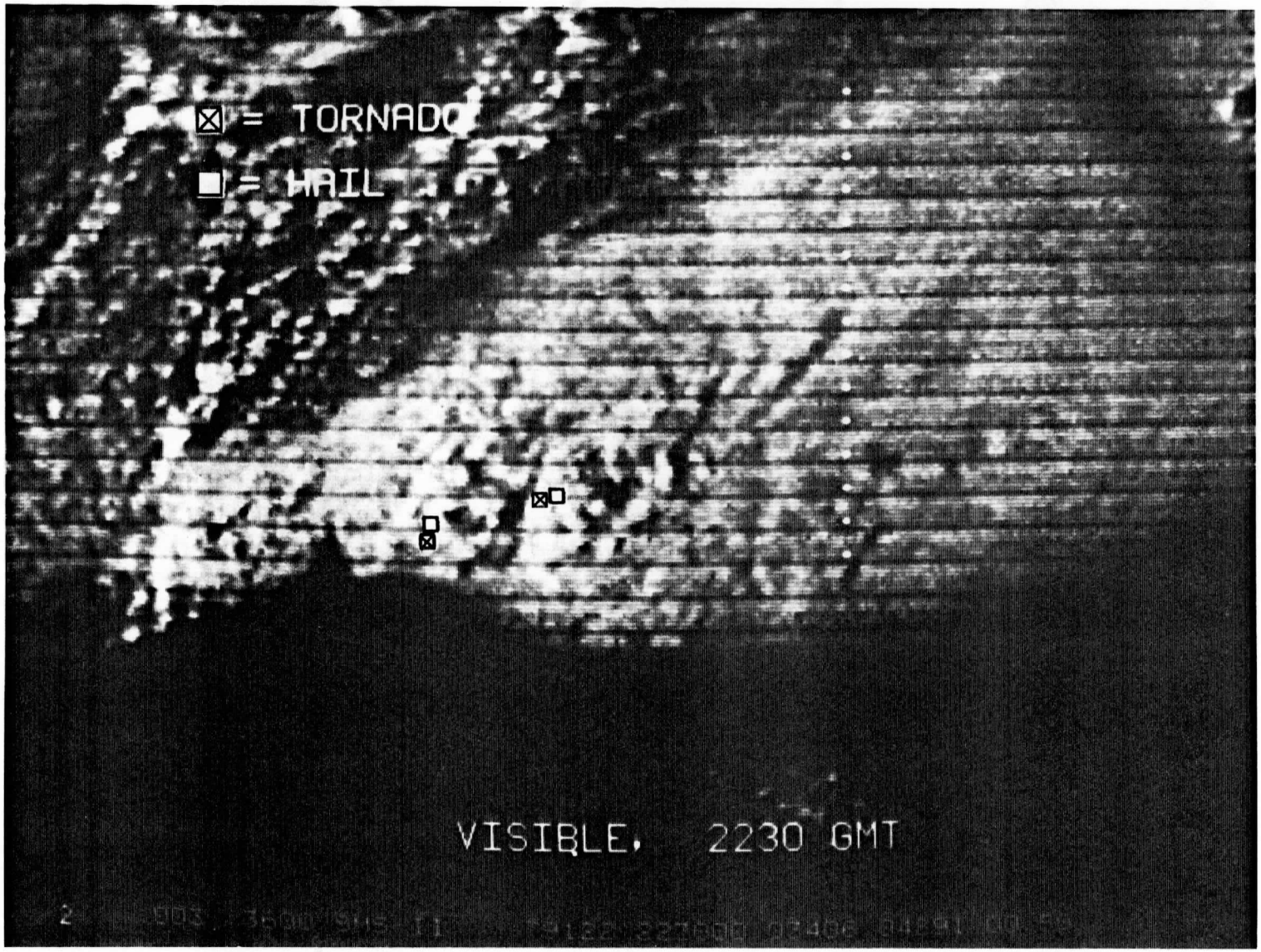

Figure 13. GOES full resolution visible image for 2230 GMT, May 2, 1979, with tornado and hail locations superimposed.

infrared, the dissipating tornado was either found on the warm or cold side of the gradient, but no longer within it (see Fig 12). Presently, we do not know whether these changes are the result of alterations of the features seen in the satellite images, such as a general collapse of nearby cloud tops, or the result of the tornado just moving away from these regions.

To summarize, the following pattern has emerged: On May 2, 1979, an infrared cold dome appeared in the southwest corner of the cloud mass. Associated with this cold dome is a sharp temperature gradient region in the infrared, forming a "V-notch" in the temperature field. Severe weather, especially tornadoes, formed on the southwest side of the gradient region. The brightest visible region (tops or clusters of tops) were coincident with the severe weather. These tops and the tornadoes moved in the same direction, with roughly the same speed. As the tornadoes began to dissipate, their location no longer corresponded to the infrared temperature gradient region and the brightest cloud tops.

6. Anvil Statistics

The statistical analyses of digital satellite and radar brightness values provide a means of comparing data sets of differing origin quantitatively. Several studies have combined and compared data from different origins: Reynolds (1979) combined digital satellite imagery, radiosondes, and surface reports to identify damaging hailstorms over the high plains; Spencer et al. (1983) correlated satellite microwave radiances with radar rain rates over land areas. On the University of Wisconsin Man-computer Interactive Data Access System (McIDAS) (Suomi et al., 1983), statistical algorithms allow for measurement and storage of the digital data, corresponding to an image displayed on the TV screen. These

statistics are often measured for part of the image enclosed within a boundary, either a standard cursor box or an irregular area drawn by the operator, on the graphics capabilities (Figure 14).

Our research explored the May 2, 1979 case using three-minute rapid scan imagery (GOES-E). The period to be discussed is from 2017 GMT to 2300 GMT. Utilizing the area statistics algorithms, we created boundaries around individual storms, and measured their areal extent. Digital brightness threshold values were determined so as to better define the edges of storms within the boundary itself. These thresholds were used to determine an inner working area, and only values brighter than the threshold value within the outline are used in the areal measurement.

The measurement of thunderstorm anvil growth is related to the intensity of a storm complex. Auvine and Anderson (1972), and Sikdar, et al. (1970) have investigated this relationship using ATS III data. Adler and Fenn (1979) measured thunderstorm intensities using SMS 2 infrared data. Our procedure, similar to those above, involved initially encircling a thunderstorm anvil with a graphics outline and setting a brightness threshold value for the anvil edge. Using a six-minute image interval, these area measurements, along with the equation, DIV = 1/A dA/dt, with A = anvil area, produced a divergence of $\sim 1.3 \times 10^{-4}$ sec^{-1} for the anvil at 2314 GMT May 2, 1979, using an IR temperature of 248°K to define the anvil edge. For tornado-producing storms utilizing a 14-minute image interval, Sikdar (1970) obtained anvil divergences on the order of 3.0×10^{-4} sec^{-1}. Auvine and Anderson (1972), for an image interval of 45 minutes, obtained thunderstorm anvil divergences of $\sim 5.0 \times 10^{-4}$ sec^{-1}. Adler and Fenn (1979) obtained mean divergences for active portions of the anvil surface of

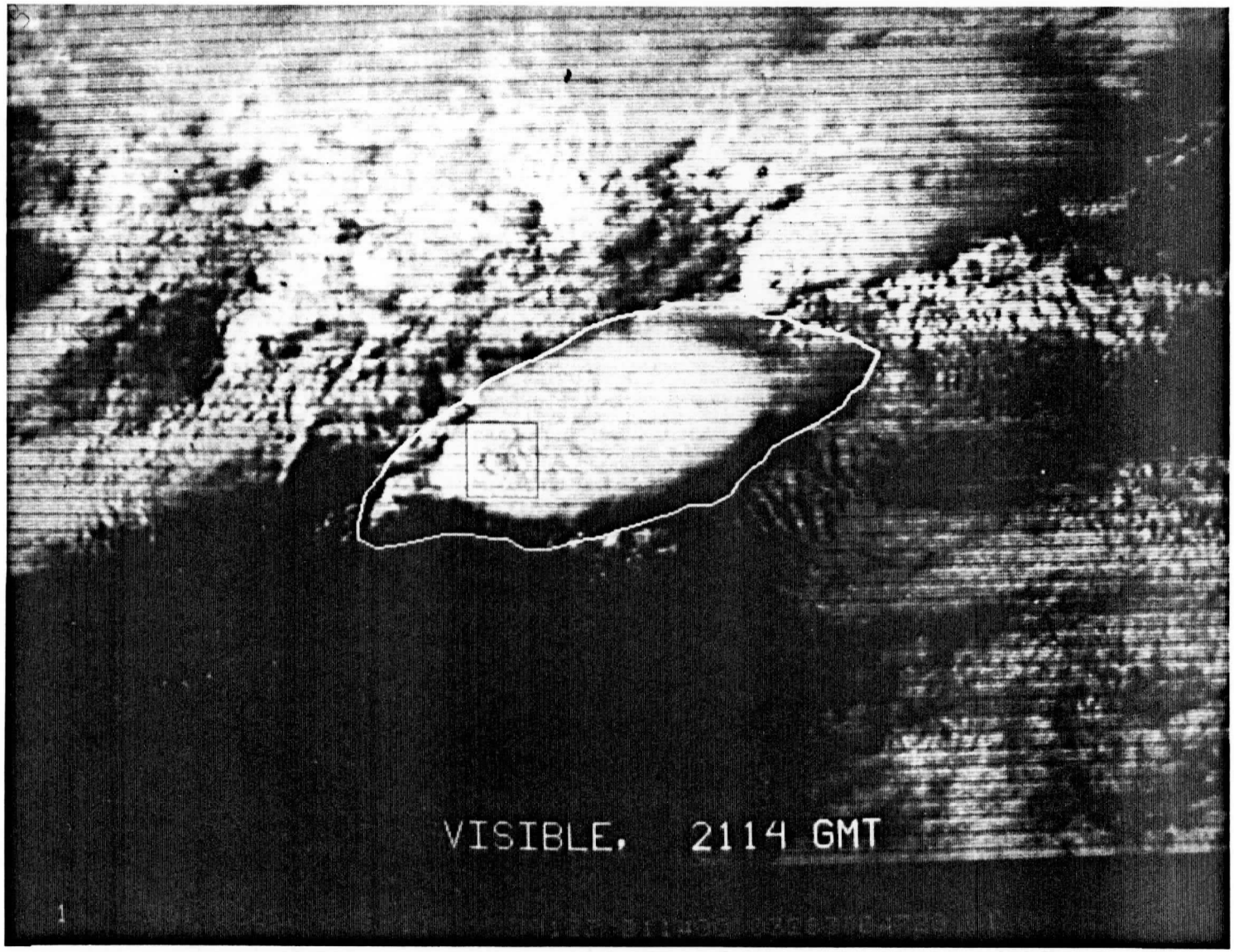

Figure 14. An operator-drawn area statistics graphics outline enclosing a thunderstorm anvil along with a graphics cursor boundary covering a portion of the inner anvil of a GOES-E visible image at 2114 GMT, May 2, 1979, over central Oklahoma.

4.5×10^{-3} sec^{-1} for severe weather-producing storms for an IR threshold area well within the outer anvil edge. Using cloud motion and radiosonde winds at 250 mb (see Section 4), divergence over the anvil of $\sim 1 \times 10^{-4}$ sec^{-1} was calculated at 2314 GMT May 2, 1979.

A second approach to linking anvil statistics to severe weather involved comparing the change of areas enclosed within specific brightness thresholds to the occurrence of severe weather beneath the anvil. We set a constant area border (i.e., a graphics cursor box), which moved with the anvil and were able to measure smaller anvil features such as individual convective centers and clusters of bright tops embedded within it. Statistics about each individual storm or storm feature may then be generated as the storm progresses in time. Entire anvil outlines may also be measured; however, problems with anvils merging with one another make it nearly impossible to compare such statistics over time.

In this study, all areal fluctuation statistics were generated using a fixed cursor border area over a portion of the anvil. As explained in the previous two sections, the overshooting tops within the anvil were grouped into clusters which could be tracked over time. On May 2, 1979, for instance, there were three such clusters in the western portion of the anvil. These clusters were followed using a cursor of about 1270 km^2, large enough to cover the area of interest, but small enough not to overlap other cluster areas. Thresholds were then chosen so as to isolate the brightest areas around and including these tops; these areas were small enough to be completely contained within the boundaries of the cursor. The box was moved from image to image to take into account the motion of the cluster. Of course, choosing appropriate thresholds that could be compared over time was a critical decision. We will explain our thresholding

shortly, in relation to the particular case studies. Areal brightness fluctuations were obtained by measuring the areas enclosed by brightnesses above various threshold values and plotting them over the image times.

There were three severe weather producing storms, as mentioned above, during the afternoon and evening of May 2, 1979 over north and central Oklahoma. Storm A produced four hail reports, one damaging wind report, and two tornadoes. Storm B produced three hail reports, one damaging wind report, and one tornado. Storm C was just forming during the latter portion of the period studied, and its severe weather was reported after this period. Alberty et al. (1979) includes a description of the severe weather locations and times for 2 May.

Areal statistics were generated from GOES-E visible images of 2 May for both the entire anvil and individual storms. Problems arose when analyzing the visible data due to the lowering solar angle during the late afternoon hours; this resulted in the brightness curves dropping off rapidly during the period when the storms were still developing and producing severe weather. Therefore, visible data was determined to be of little use on May 2 for the statistical measurements except during the incipient stages of storm development. Normalized visible images were not feasible due to the large time difference between local noon and the period of storm maturity.

Digital infrared imagery from GOES-E was analyzed for May 2, and the threshold curves maintained a promising consistency throughout the latter portions of the period. In the infrared, the statistics algorithms allow for the threshold determinations to be made in terms of temperature (°Kelvin). On a digital brightness scale of 0 - 255 for IR images, temperature and brightness are related by:

$$t = 418 - b \qquad (b > 176)$$

$$t = 330 - (b/2) \qquad (b \leq 176)$$

where t is temperature (°K) and b is brightness (0 - 255).

These relationships assume that the earth's surface and surrounding atmospheric features are blackbody radiators, which is not necessarily the case (Mosher, 1979). In addition, GOES-E infrared resolution at the satellite subpoint is approximately 4 km. This resolution averages out the smaller features of a thunderstorm anvil surface such as a small dome or turret. At the anvil edge, evaporation processes may also bias the true radiance sensed by the satellite. In spite of these constraints, and the fact that IR sensed blackbody temperatures are not the same as the true cloud temperatures, it was still feasible to select a series of blackbody temperatures from 212°K to 204°K which could at least crudely reflect the areal growth within the anvil over time.

Figure 15 shows the coldest counts for Storm A from 2047 to 2253 GMT. Observations for each threshold were plotted on a time series graph, with curves drawn where consecutive observations were made. Isolated measurements are represented as singular points.

The three-minute rapid scan interval could not be preserved for all periods of measurement due to satellite time interval image gaps, as well as missing, or noisy data. Image time gaps in excess of 10 minutes were present on several occasions. Observations of short term fluctuations in the areal curves near the time of occurrence of a surface severe weather event were thus not always possible.

Figure 15 shows the overall change of each areal threshold curve as a function of time. Fluctuations can be observed on each curve, especially at the shorter measurement intervals. To obtain a general trend of each

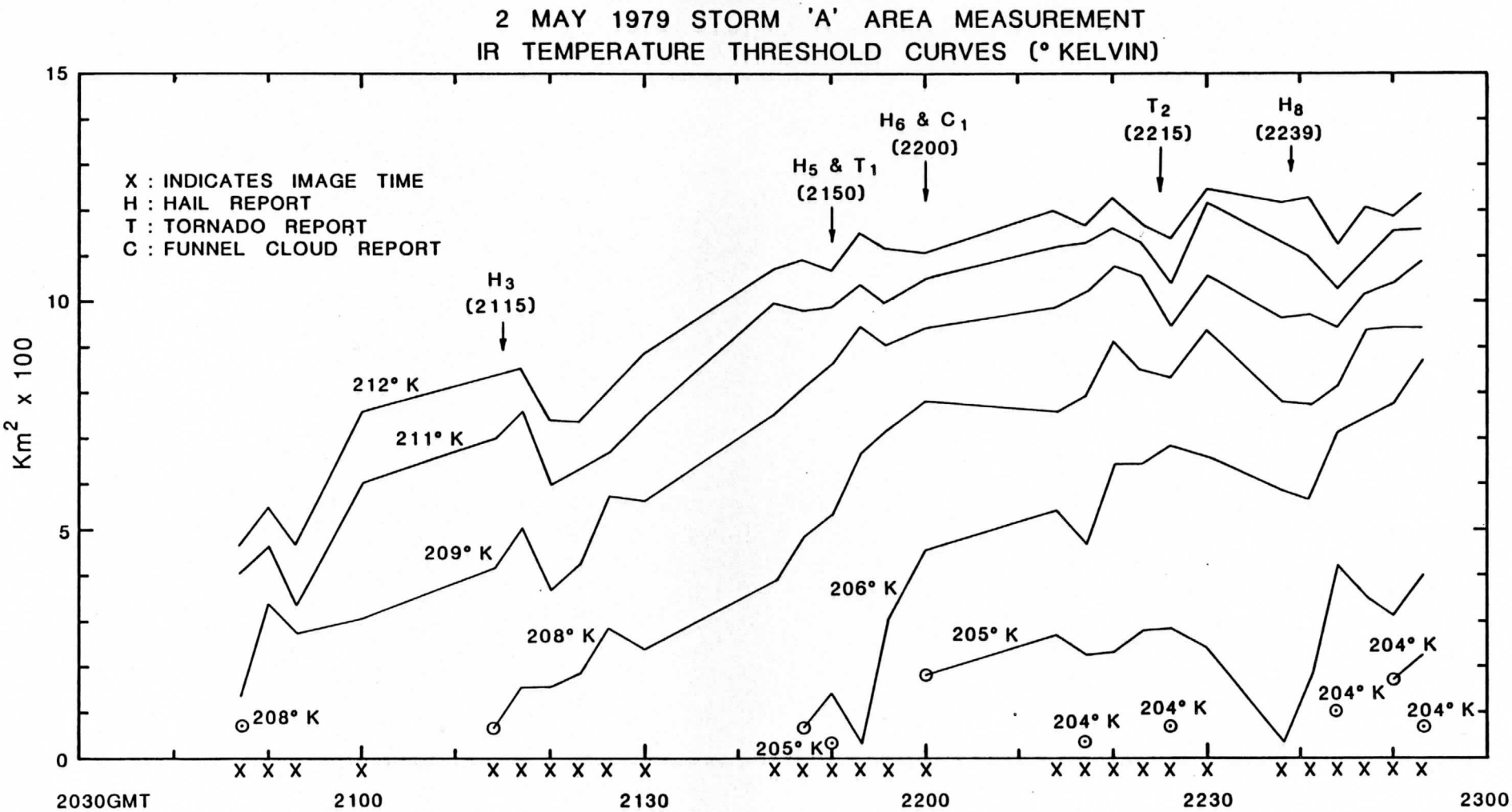

Figure 15. IR temperature threshold curves during Storm A over central Oklahoma, May 2, 1979.

curve near the time of a severe weather event, a line passing through the points where each curve intersected the beginning and end of a 10-minute interval was drawn. Three 10-minute intervals were chosen for each severe weather event: one beginning, another ending, and a third centered on the event. Individual storms corresponding to severe weather events were isolated on the satellite image by first identifying the cluster of overshooting tops at the anvil surface and then plotting the locations of the surface events on the image.

Table 3 summarizes the slopes of these curves for Storm A. To insure a measure of integrity throughout the period, endpoints of the 10-minute trends were required to fall within ± 2 minutes of an image measurement time. This requirement was implemented due to the temporal inconsistency of the satellite image sampling. Trends which do not satisfy this requirement are noted in the table. Each noted segment had only one endpoint out of range, with the maximum being 5 minutes. Failure to meet this requirement does not necessarily mean that the trend measured was false.

Concerning only the tornado (#1 and 2) and funnel cloud (#1) reports for Storm A, all curves show a growth tendency 10 minutes prior to the event. Except for the 205°K curve, the same positive tendency holds true for the interval ± 5 minutes to the event. For the period 10 minutes after the event, the pattern is not as decisive, although increases are still generally indicated. For the hail reports, no definite overall curve tendency is apparent. Hail (#3 and 8) essentially contradict one another in their tendencies.

Where three-minute image measurements are proximate to severe events (Figure 15), relative short term curve fluctuations are noted. For H_3 and

Reported Severe Event	Temperature Curve (°K)	10 Minutes Prior to Event	± 5 Minutes to Event	10 Minutes After Event
Hail #3 at 2115 GMT	212	+*	−*	−
	211	+*	−*	−
	209	+*	−*	+
	208			+
	206			
	205			
Hail #5 and Tornado #1 at 2150 GMT	212	+*	+	+
	211	+*	+	+
	209	+*	+	+
	208	+*	+	+
	206			
	205			
Hail #6 and Funnel Cloud #1 at 2200 GMT	212	+	+*	+*
	211	+	+*	+*
	209	+	+*	+*
	208	+	+*	−*
	206	+	+*	−*
	205			+*
Tornado #2 at 2215 GMT	212	+*	+*	−
	211	+*	+*	−
	209	+*	+*	−
	208	+*	+*	+
	206	+*	+*	+
	205	+*	−*	+
Hail #8 at 2239 GMT	212	−	−*	−
	211	−	−*	+
	209	−	−*	+
	208	−	−*	+
	206	−	+*	+
	205	−	+*	+

- indicates curve ascent
- indicates curve descent
NC indicates no change
* indicates that at least one endpoint of a 10-minute trend is not within ± 2 minutes of an image measurement

Table 3.

10 Minute Trend in IR Temperature Threshold Curve for Storm A, May 2, 1979

T_1, three-minute fluctuations in excess of 100 km^2 occur for the coldest curves nearest each event time. Fluctuations for H_3 and T_2 were not as great. T_2 shows a decline in the coldest curves near the time of the initial report. This possibly is associated with the satellite sensing warmer temperatures above the tropopause indicative of a portion of the anvil rising above the tropopause. Soundings taken at 2300 GMT May 2 and 00 GMT May 3 indicate the tropopause height near 13 km, lower than the 13.6 km to 15.9 km maximum cloud heights measured by Hasler (1981) at 2215 GMT.

Figure 16 shows the coldest curves (corresponding to the highest tops) for Storm B for the period 2130 GMT to 2253 GMT for May 2. As with the curves for Storm A, an overall increase with time is evident for all curves. The major departure is seen between 2230 GMT and 2240 GMT when a majority of the curves reach a peak. During this period, T_3 contained a multiple vortex structure and had a wide (2 mile) track. The curves then fall off sharply during the 10-minute interval prior to the dissipation of T_3; rapid growth then follows.

Short term three-minute fluctuations were found near the touchdown of T_3, and the dissipation of H_7, and T_3. These three-minute fluctuations indicate a temporal lag in the curves during the period 2235 to 2250 GMT. The 212°K to 209°K curves reach a peak near 2238 GMT, while the 206°K and 205°K curves reach their peak three minutes later. The same pattern is also evident six minutes later when the curves reach a minimum. It is difficult to offer a physical explanation of this behavior, given the fact that it is the warmer curves that stop or start their growth first. It is possible that the two sets of curves are being influenced by local effects of cloud tower growth and decay which may or may not be related to one

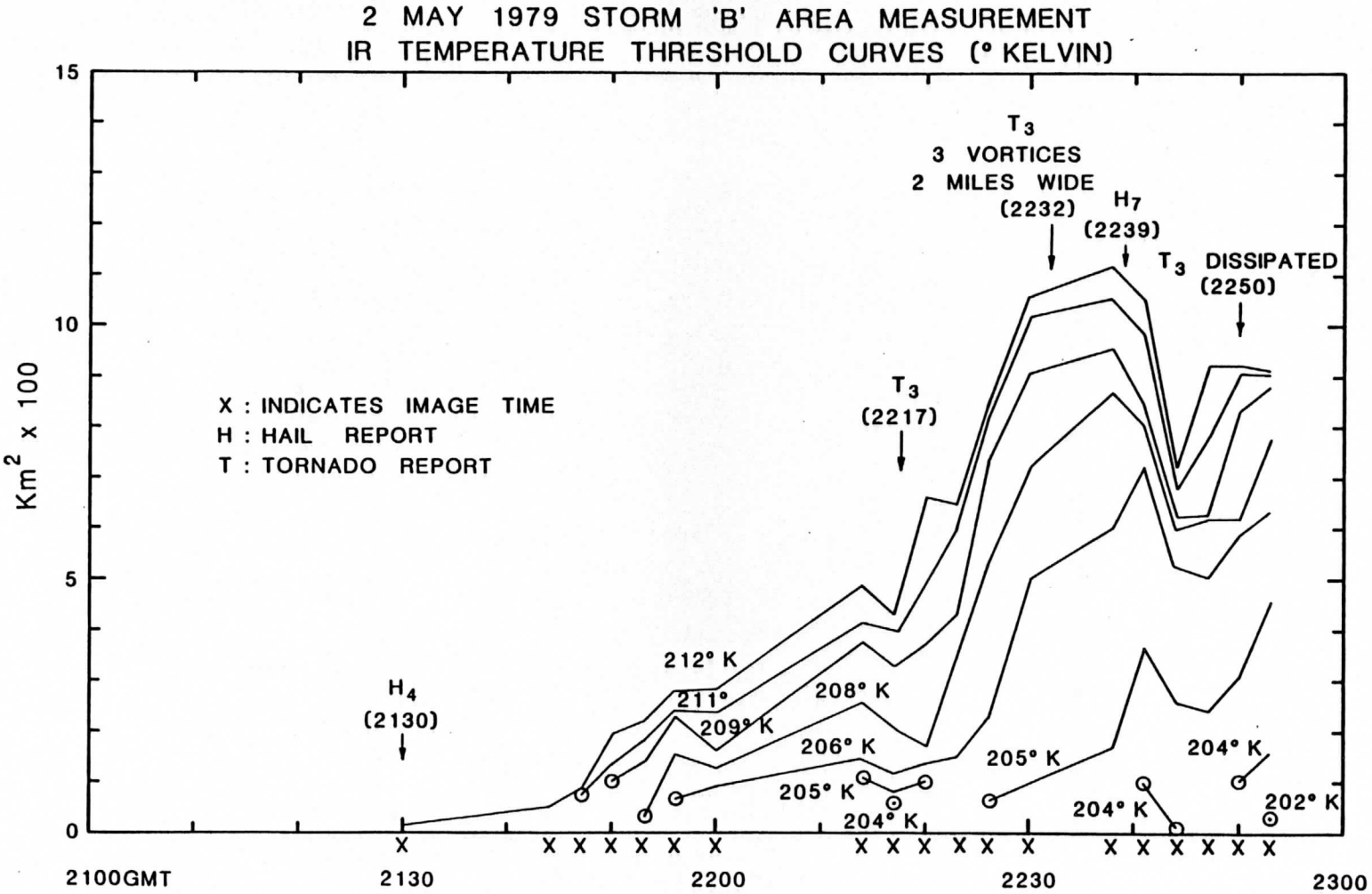

Figure 16. IR temperature threshold curves during Storm B over central Oklahoma, May 2, 1979.

another. It is also possible that the large interval between measurements masks other important fluctuations here.

Table 4 shows the 10 minute trends for the curves of Storm B. As with Storm A, the majority of curves have a positive slope from 10 minutes prior to the T_3 touchdown to the point where T_3 contained a two-mile wide track at 2232 GMT. An interesting reversal is evident, beginning at 2242 GMT. A majority of curves descend, with only the 206/205°K curves having a positive slope. The one hail event reported shows behavior similar to Hail #3 in Storm A.

The areal curves of the IR satellite sensed temperature for Storms A and B exhibit several consistent patterns. The first one is the overall positive growth before and during the first sightings of tornadoes and funnel clouds; no pattern is apparent for the hail reports, however. The majority of 10-minute threshold curve trends also have a positive slope prior to and during an initial tornado or funnel report. Second, immediately after tornadic events, the slope of some of these curves reverses. An exception is Storm A's T_1, which continued to show growth at all thresholds. This behavior could be the reflection of a cloud top collapse (in the case where the coldest thresholds show decline -- Funnel Cloud #1) or of a general decrease in mass flux into the anvil (causing decreases in some of the warmer threshold areas where evaporation and sinking might take their toll -- T_2, T_3).

When considering the short term three-minute interval threshold curve fluctuations, descent of the coldest curves near the initial reports of T_1, T_2, and T_3 possibly indicates vertical cloud ascent beyond the tropopause, with the satellite sensing warmer IR temperatures. In addition, a lag

Reported Severe Event	Temperature Curve (°K)	10 Minutes Prior to Event	± 5 Minutes to Event	10 Minutes After Event
Tornado #3 at 2217 GMT	212	+*	+	+
	211	+*	+	+
	209	+*	+	+
	208	+*	+	+
	206	NC*	+	+
	205			
Tornado #3 3 Vortices Track 2 Miles Wide at 2232 GMT	212	+	+	-
	211	+	+	-
	209	+	+	-
	206	+	+	+
	205			
Hail #7 at 2239 GMT	212	+	-*	-
	211	+	-*	-
	209	+	-*	-
	208	+	-*	-
	206	+	-*	-
	205	+	+*	+
Tornado #3 Dissipates at 2250 GMT	212	-		
	211	-		
	209	-		
	208	-		
	206	-		
	205	+		

+ indicates curve ascent
- indicates curve descent
NC indicates no change
* indicates that one endpoint of a 10-minute trend is not within ± 2 minutes of an image measurement

Table 4

10-Minute Trend in IR Temperature Threshold Curves for Storm B, May 2, 1979

between the times when the coldest and the warmest reached their minima or maxima was noted.

The short term three-minute interval measurements reveal rapid fluctuation in the curves that otherwise would not be detected from longer scanning intervals. Under normal operations, the GOES satellites have a standard 30-minute scanning interval, even though the lifetimes of a majority of severe weather events occur well within this 30-minute time frame. In addition, spatial resolutions of the satellite sensors (1 km VIS, 4 km IR) usually exceed the dimensions of smaller thunderstorm anvil features such as turrets and domes (Umenhofer, 1975). Hence, increased satellite resolution in both time and space would be highly beneficial in developing and testing quantitative measurement techniques that concentrate on these smaller scale morphological features of severe local storms.

7. Software Improvements

In order to effectively analyze and integrate data, software was written to reformat tapes to a common file structure. Generally speaking, this meant observed phenomena (temperature, pressure, etc.) at a specific time and location would be stored in SDS files, and image data (radar, satellite pictures) would be stored in image data files in the satellite projection. Also, some specialized software was written to complement the general McIDAS capabilities. The following pages describe the software developed for this project in the McIDAS documentation format. This includes key-in syntax, description of parameters, and an explanation of how the program works. For more details, refer to the McIDAS Users' Manual, available from SSEC.

COMMAND: Read digital radar data from tape PROGRAM: RADAR 2

COMMAND FORMAT:

RADAR 2 area time nelv itap file inc iopt mult.

PARAMETER DESCRIPTION:

1. area: First digital area to load data into. If area is ϕ, then a list of the file contents is printed (elevation angle, beginning and ending azimuths, and time).

2. time: First time to read from tape (must have gotten a list of file contents as described above).

3. nelv: Number of elevation angles to read, which will be stored in successive areas.

4. itap: Tape number. Not used except for header on printout.

5. file: File number to read on tape (default = 1).

6. inc: Increment in degrees between azimuths to store data. If inc is less than data spacing, averaging between lines is done (default = 1). Data spacing is every 2°.

7. iopt: If this parameter is non-zero, debug messages are printed (default = ϕ).

8. mult: A multiplication factor to scale the digital data (default = 1).

EXPLANATION:

This program reads NSSL WSR-57 digital radar tapes and puts this information in digital areas; each line is an azimuth. The data are in Dbz's and are calibrated to account for power transmitted, range, and atmospheric attenuation. See RADCAP, RADRHI, PPIMAP to process this data into satellite projection images.

NOTE: 1. Typing the 'G' key will terminate the program

2. Appending the key-in with 'PR' will send output text to a printer.

COMMAND: Read PAM data from tape PROGRAM: PAMRDE

COMMAND FORMAT:
PAMRDE

PARAMETER DESCRIPTION:
None

EXPLANATION:
FSU-generated PAM data tapes are read into an SDS file. All parameters are stored. The SDS file (type = PAM) must be generated (allowing 165 sectors/hour of data) and pointed to (JX command). The entire file is read, and the program will terminate if the SDS file fills or the 'G' key is typed. (Use XC to display on grid data.)

PAM SDS file structures

1. Each element contains one hour of data (165 sectors).

2. Keywords
IDN = identification number
DAY = day of month
TIM = GMT time (HHMMSS)
LAT = latitude (deg*10000)
LON = longitude (deg*10000) west positive
T = temperature (Kelvin*100)
TD = dewpoint (Kelvin*100)
TW = wet bulb temperature (Kelvin*100)
RH = relative humidity (percent*100)
PRE = pressure (mb*10)
RFL = rainfall rate (mm/hr*100)
U = U-comp of wind (m/s*100)
V = V-comp of wind (m/s*100)
GUS = wind gusts (m/s*100)

COMMAND: Read QueenAire or Sabreliner tapes PROGRAM: ACREAD

COMMAND FORMAT:

```
ACREAD  sds  aircraft  yyddd  file
```

PARAMETER DESCRIPTION:

1. sds: SDS file to write data (program generates it).

2. aircraft: 'QUE' for QueenAire, 'SAB' for Sabreliner.

3. yyddd: year-day of flight.

4. file: tape file to read.

EXPLANATION:

NCAR generated aircraft data are read into an SDS file (type = AC). The entire file is read, and the program will terminate if the SDS file fills or the 'G' key is typed.

NOTE: This program reads a 9-track tape that has been copied from a 7-track tape (the data were not packed, so there are two extra bits per 8 bit field). Use XC to display or grid data.

AC SDS file structure

keywords:

DAY = day (YYDDD)
TIM = time GMT (HHMMSS)
LAT = latitude (deg*10000)
LON = longitude (deg*10000)
Z = height (m*100)
T = temperature (Kelvin*100)
TD = dew point (Kelvin*100)
HUM = absolute humidity (g/m^3*100)
Q = mixing ratio (g/kg*100)
TLC = temp of LCL (Kelvin*100)
PLC = pressure at LCL (mb*10)
THA = potential temp (Kelvin*100)
THE = equiv potential temp (Kelvin*100)
THV = virtual potential temp (Kelvin*100)
U = U-comp of wind (m/s*100)
V = V-comp of wind (m/s*100)
W = W-comp of wind (m/s*100)
DIR = wind direction (deg*100)
SPD = wind speed (m/s*100)
ATT - attach angle (deg*100)
SSL = sideslip angle (deg*100)
UG = U-comp of wind gust (m/s*100)
VG = V-comp of wind gust (m/s*100)
WG = W-comp of wind gust (m/s*100)
UX = wind vector long gust comp (m/s*100)
VY = wind vector lat gust comp (m/s*100)
THI = aircraft true heading (deg*100)

GS = ground speed (m/s*100)
TAS = true air speed (m/s*100)
PIT = aircraft pitch attitude (deg*100)
ROL = aircraft roll attitude (deg*100)
YAW = aircraft true heading (deg*100)
VZI = instrument vert vel (m/s*100)
PB = dynamic pressure (mb*10)
PBC = corrected dynamic press (mb*10)
PS = static pressure (mb*10)
PSC = corrected static press (mb*10)
WP3 = damped aircraft vert vel (m/s*100)
HI3 = pres damped inertial alt (m*100)
UX1 = wind vector long comp (m/s*100)
VY1 = wind vector lat comp (m/s*100)

COMMAND: READ VAS/AVE into RAOB file PROGRAM: RAOGSW

COMMAND FORMAT:

RAOGSW sds* ntim begtim inc nfiles$_{cr}$

COMMAND DEFAULT:

None

PARAMETER DESCRIPTION:

1. sds# = sds file number. Must be generated on disk.

2. ntim = # of time periods (defaults to 8).

3. begtim = time in days, hours, minutes (DDHHMM).

4. inc = increment between times in hours.

5. nfiles = number of files to read from tape (defaults to 1).

EXPLANATION:

Reads VAS/AVE Raob tapes into Raob SDS file.

NOTE: SDS file must be generated on disk before executing job.

COMMAND: Enter or List Severe Weather Report PROGRAM: FILSVR

COMMAND FORMAT:

1. FILSVR time lat lon z wx (enter severe weather)

2. FILSVR time lat lon z wx 'com' (enter severe weather with comment)
   FILSVR * text

3. FILSVR 'LIS' beg end key (list severe weather)

PARAMETER DESCRIPTION:

1. time: time of weather event (hh00 GMT)

2. lat, lon: latitude, longitude location (DDDMMSS) west negative

3. z: parallax height of lat/lon (see SVRPAR)

4. wx: severe weather report from SESAME Operations Manual (T1, W6, H4, C3 for example)

5. text: text description of severe weather (up to 24 characters)

6. beg: beginning record number in SDS file to list

7. end: ending record number in SDS file to list

8. key: type of severe weather to list (T will list any weather parameter beginning with letter T)

EXPLANATION:

This program is used to enter severe weather reports from the SESAME Operations Manual and list the data. Form #1 enters the data into the file. Form #2 enters the data with the mandatory second key-in entering additional text (up to 24 characters). Form #3 lists the SVR SDS file. The file must be JX'd.

SVR SDS File Structure

Keywords

```
DAY        = day (YYDDD)
TIM        = time GMT (HHMMSS)
LAT        = latitude (deg*10000)
LON        = longitude (deg*10000)
Z          = altitude of lat/lon (parallax adjustment)
WX         = severe weather report (3 characters)
XTA → XTH  = 24 characters of text
XTI → XT3  = unused
```

COMMAND: Remap Radar to GOES Projection or RHI PROGRAM: PPIMAP

COMMAND FORMAT:

```
PPIMAP  inarea  outarea  spline  alt   (PPI,CAPPI)
PPIMAP  inarea  outarea  opline  line  ele  height  range  (RHI)
```

PARAMETER DESCRIPTION:

1. inarea: input area, generated by RADAR2 for PPI, by RADCAP for CAPPI, or by RADRHI for RHI.

2. outarea: satellite area to contain radar (must be generated).

3. spline: spline size in remap image, valid size = 6, 12, 21, 24, 42, 48. (Default = 12.)

4. alt: altitude in meters (in order to add satellite viewing parallax so that clouds and radar will overlay. Default for PPI = 0, default for CAPPI is the CAPPI height.)

The following apply only to RHI:

5. line: line extents of the form (bbbeee: bbb = beginning, eee = ending); bbb is the image line for the ground; eee is the image line for the top.

6. ele: element extents of the form (bbbeee).

7. height: height in km, corresponding to the line extents.

8. range: range in km, corresponding to the element extents.

EXPLANATION:

This program takes areas generated by RADAR2 and remaps them to a PPI, by RADCAP to a CAPPI, and by RHORHI to a RHI. The CAPPI and PPI are in the satellite projection, and the RHI in a range vs. height display. Valid spline sizes: 6, 12, 21, 24, 42, 48. As smaller spline sizes are used, the amount of interpolation in the remapped image is reduced, but computation time is increased. It was determined, for visual examination, that a spline of 12 for PPI or CAPPI and 6 for RHI gave good results in a reasonable amount of time.

NOTE: For RHI, the beginning line (ground) will be larger than the ending line (top).

COMMAND: Read MSFC IBM RAOB into RAOB file PROGRAM: RAOIBM

COMMAND FORMAT:

RAOIBM sds# ntim begtim inc nfiles$_{cr}$

COMMAND DEFAULT:

None

PARAMETER DESCRIPTION:

1. sds# = sds file number. Must be generated on disk.

2. ntim = # of time periods (defaults to 8).

3. begtim = beginning time in days, hours, minutes (DDHHMM).

4. inc = increment between times in hours.

5. nfiles = number of files to read from tape (defaults to 1).

EXPLANATION:

Reads MSFC IBM Raob tapes into Raob SDS file on disk. If "ntim" is > than 8, the Raob SDS file must be made larger by approximately 800 sectors for each additional time.

NOTE: SDS file must be generated on disk before executing job.

COMMAND: Alter Lat/Lon in SDS File
to Adjust for Satellite Parallax

UD-05 2/83
PROGRAM: PSHIFT

COMMAND FORMAT:

PSHIFT insds outsds height$_{cr}$

COMMAND DEFAULT PARAMETERS:

None

PARAMETER DESCRIPTION:

1. insds = input SDS file number (use CURELE for this file).

2. outsds = output SDS file number (generated by program and element time is assigned input height).

3. height = height in meters to shift for parallax to bring ground measurements to a cloud level. (If height is negative, takes from cloud to ground.)

EXPLANATION:

PSHIFT changes LAT/LON in SDS file to introduce parallax shift to take ground measurements to a specified cloud level. The element time of the output SDS file is assigned the height.

COMMAND: Parallax adjust lat/lon in SVR SDS file PROGRAM: SVRPAR

COMMAND FORMAT:

SVRPAR insds outsds ht

PARAMETER DESCRIPTION:

1. insds: input SDS file number

2. outsds: output SDS file number (program generated)

3. ht: height in meters for parallax correction.

EXPLANATION:

The height input is placed in the keyword 'Z' of the SVR SDS file and also the element of the output SDS file. The program works on the current element of the input SDS file.

COMMAND: Stereo height calculation PROGRAM: PARLAX

COMMAND FORMAT:

PARLAX ss mode estht iter

PARAMETER DESCRIPTION:

1. ss: satellite number of west satellite

2. mode: not currently used

3. estht: estimated height (m) (default = 10000)

4. iter: number of iterations (default = 10)

EXPLANATION:

Two digital images coincident in time and space are retrieved, one from each satellite. One of the images (usually the West) is remapped into the satellite projection of the other using GOSMAP. The images are visually juxtaposed, and alternately displayed on the screen. The locations of cloud elements common to both images are indicated by an operator controlled cursor in velocity mode ('V' key). Keying in PARLAX twice in succession results in an estimated height derived from the parallax shift.

COMMAND: Contour Brightness or IR Temperatures UD-05 2/83

(Graphics Overlay Image) PROGRAM: TVTOUR

COMMAND FORMAT:

TVTOUR int color option min size label$_{cr}$

COMMAND DEFAULT PARAMETERS:

TVTOUR int 1 0 0 6 1$_{cr}$

PARAMETER DESCRIPTION:

1. int = contour interval.
2. color = color (1-7).
3. option = 0 for digital brightness contours,
   = T for IR temperature contours.
4. min = minimum brightness to contour.
5. size = size of labels on contours.
6. label = label interval (1 = every contour; 2 = every other contour ...).

EXPLANATION:

TVTOUR contours displayed digital data within a square cursor. An area up to 100x100 points can be contoured. For images displayed without magnification, the cursor is limited to 100x100, but for a 4X blowup image, the cursor can be up to 400x400.

COMMAND: Dynamic vector analysis PROGRAM:WINPLT

COMMAND FORMAT:

WINPLT time station vector

PARAMETER DESCRIPTION:

1. time: Raob day/time ddhh00

2. station: Raob station id

3. vector: record number of wind vector in SDS file (JX'd) for comparison with RAOB.

EXPLANATION:

This program graphically compares an input wind vector with a radiosonde wind profile. The wind vector is plotted and as the joysticks are moved up and down along the pressure scale, the radiosonde wind is replotted. Current level, speed, direction for both vectors are displayed at the top of the screen. Agreement between vectors is determined visually. To stop program, type 'Q'.

COMMAND: Graphics Height vs. Range Scale PROGRAM:RHIPLT

COMMAND FORMAT:

RHIPLT line ele height range options

PARAMETER DESCRIPTION:

1. line, ele, height, range: these parameters must be the same as what was keyed in for PPIMAP.

2. options: any or all of the following may be used:

HGT n : n is the digit scale height (default = 7).

TIC n : n is the length of the tic marks (default = 10).

DX n : n is the number of divisions in the range direction.

DY n : n is the number of divisions in the height direction.

SUB n : n is the number of subdivisions (default = 1).

EXPLANATION:

This program overlays a RHI image (from PPIMAP) with a graphics range-height scale.

COMMAND: List or Time-Series Plot of PAM Data PROGRAM: PAMLIS

COMMAND FORMAT:

1. PAMLIS begtim endtim (list all stations)
2. PAMLIS 'ID' id begtim endtim (list station = id)
3. PAMLIS 'ID' id begtim endtim 'PLO' key inc
   (time-series plot)

PARAMETER DESCRIPTION:

1. begtim: beginning time on ddhh00

2. endtim: ending time (default = begtim)

3. id: station id number

4. key: parameter to plot (T, TD, TW, RH, PRE, RFL, U, V, GUS)

5. inc: increment in minutes for plot (default = 1).

EXPLANATION:

This program lists the contents of a PAM SDS file (JX'd) in tabular form (#1,2) or graphically displays a time-series plot of a parameter (for up to 1 hour) (#3).

8. Summary

We have described the progress made over the past few years using satellite and other data to study several SESAME severe storm days. At the outset, we had hoped to accomplish a wide-ranging case study of the mesoscale motions near each of the storms, using cloud, radar, and conventional data. In terms of the combination and display of these data along with the necessary technique development, our efforts were successful. Unfortunately, delays in receiving data, along with unexpected data quality problems, made processing difficult and time consuming. Although the piecemeal results presented here have an intrinsic interest, we were prevented from spending the time necessary to tie various results together and pursue promising research leads.

To reach our goal of producing complete and meaningful data sets, we combined satellite image data with rawinsondes, high density surface observations, digital radar, aircraft, plus other derived quantities. This allowed us to view the atmosphere on a variety of time and space scales and from several different points of view simultaneously. This approach has proven data processing intensive.

Because of the time and money involved in some of these activities, we have pointed out in a number of places the need for caution: The researcher should be aware, for example, of the difficulties in producing a high quality wind set and the likely benefits of such work.

Summarizing our results, two high resolution wind sets were produced for May 2. We found a very favorable environment for severe weather development: There was favorable vertical shear; the developing cells propagated into the warm moist air; there was a surface front that moved into the area of interest; we found divergence at high levels, and convergence near the surface; there was a short wave at about 500 mb; using

isentropic surfaces, we found evidence of upward motion and moisture convergence. Though many of these results were also indicated on conventional synoptic analyses, our analyses had the advantage of a high space and time resolution, making them more immediately applicable to the storm area.

We were able to track the motions of small-scale features on the anvil surface. These overshoots have motion comparable to that of tornadoes at the surface or radar echoes; they do not move with the environmental wind field. We also located and tracked other small-scale features whose motion differed both from the environmental winds and the overshooting tops.

The severe weather formed in the infrared temperature gradient region along the edge of the cold domes. In our cases, these domes occurred on the southwest side of the anvil. In addition, the severe weather was coincident with the brightest (deepest) areas in the visible images. When the severe weather at the surface began to dissipate, it moved away from the bright visible, and infrared gradient area.

We were also able to measure the growth of the anvils both in general area, and in terms of their brightest regions. To accomplish all of the above, a great deal of software for McIDAS was produced and documented.

Although progress was made on all of our goals, much more research in this area needs to be undertaken. First, more case studies should be performed to try and generalize our results. Second, the area of research that appears to have the most promise is the study of small-scale features on the anvil surface, including their motion, statistics and morphology. This could lead to an empirical measure of the potential for a storm's severity. Finally, there should be more research directed at distinguishing severe from non-severe storms, using modern satellite technology.

REFERENCES

Adler, R.F., and D.D. Fenn, 1979: Thunderstorm intensity as determined from satellite data, J. Appl. Meteor., 18, 502-517.

Alberty, R.L., D.W. Burgess, C.E. Hare, J.F. Weaver, 1979: SESAME 1979 Operations Summary, Env. Res. Lab., U.S. Dept. Comm., Boulder, CO, 253 pp.

Anderson, C.E., 1979: Anvil outflow patterns as indicators of tornadic thunderstorms, Preprints, 11th Conference on Severe Local Storms, Amer. Meteor. Soc., Boston, 481-487.

Anderson, C.E., 1982a: Cycloidal path exhibited by the mesocyclone associated with the Wichita Falls tornado imagery, Preprints, 12th Conf. Severe Local Storms, Jan. 12-15, 1982, Amer. Meteor. Soc., Boston, 503-505.

Anderson, C.E., 1982b: Dramatic development of thunderstorm circulation associated with the Wichita Falls tornado as revealed by satellite imagery, Preprints, 12th Conf. Severe Local Storms, Jan. 12-15, 1982, Amer. Meteor. Soc., Boston, 493-498.

Auvine, B., and Anderson, C.E., 1972: The use of cumulonimbus anvil growth data for inferences about the circulation in thunderstorms and severe local storms, Tellus, 24, 300-311.

Barnes, S.L., 1973: Mesoscale objective map analysis using weighted time series observations, NOAA Tech. Memo. SRL-NSSL-62, 60 pp.

Bluestein, H.B., E.K. Berry, J.F. Weaver, and D.W. Burgess, 1980: The formation of tornadic storms in northwestern Oklahoma on 2 May 1979, Preprints, Eighth Conference on Weather Forecasting and Analysis, Amer. Meteor. Soc., Boston, 57-62.

Fujita, T.T., 1972: Tornado occurrences related to overshooting cloud-top heights as determined from ATS pictures, Satellite and Mesoscale Research Project, No. 97, U. Chicago, 29 pp.

Fujita, T.T., 1982: Infrared, stereo-height, cloud-motion, and radar-echo analysis of SESAME-day thunderstorms, Preprints, 12th Conf. Severe Local Storms, Jan. 12-15, 1982, Amer. Meteor. Soc., Boston, 213-216.

Goodman, H.M., Auvine, B., and Santek, D., 1982: The relationship of satellite and radar storm signatures to the subsynoptic wind field, Preprints, 12th Conf. Severe Local Storms, Jan 12-15, 1982, Amer. Meteor. Soc., Boston, 217-220.

Hasler, A.F., 1981: Stereographic observations from geosynchronous satellites: an important new tool for the atmospheric sciences, Bull. Amer. Meteor. Soc., 62, 194-212.

Mosher, F.R., 1976: Cloud height determination, Proceedings of the Symposium on Meteorological Observations from Space: Their Contribution to the First GARP Global Experiment, 19th Meeting of COSPAR at Philadelphia, PA, NCAR, Boulder, CO, 201-204.

Mosher, F.R., 1979: Cloud drift winds from geostationary satellites, Atmos. Tech., 10, 53-60.

Negri, A.J. and T. VonderHaar, 1980: Moisture convergence using satellite-derived wind fields: A severe local storm case study, Mon. Wea. Rev., 108, 1170-1182.

Newton, C.W., and H.R. Newton, 1959: Dynamic interactions between large convective clouds and environment with vertical shear, J. Meteor., 16, 483-496.

Pearl, E.W., W.E. Shenk, and W. Skillman, 1975: Cloud top parameters -- a hail indicator, Preprints, 9th Conf. Severe Local Storms, Amer. Meteor. Soc., Boston, 464-467.

Reynolds, D.W., 1979: Observations and detection of damaging hailstones from geosynchronous satellite digital data. Preprints, 11th Conf. Severe Local Storms, Amer. Meteor. Soc., Boston, 217-220.

Shenk, W.E., 1974: Cloud top variability of strong convective cells, J. Appl. Meteor., 13, 917-922.

Sikdar, D.N., Suomi, V.E., and Anderson, C.E., 1970: Convective transport in mass and energy in severe storms over the United States -- an estimate from a geostationary altitude, Tellus, 22, 521-532.

Spencer, R.W., Martin, D.W., Hinton, B.B., and Weinman, J.A., 1983: Satellite microwave radiances correlated with radar rain rates over land. Submitted to Nature.

Suchman, D., B. Auvine, R. Lord, D. Martin, F. Mosher, and D. Santek, 1981: Improvements in the Use of Meteorological Satellite Data: Some Techniques Developed for GATE, Space Sci. and Engr. Center (SSEC), Madison, WI.

Suchman, D., and G.J. Krause, 1979: The determination of height variations in overshooting thunderstorms from geostationary satellite images, Preprints, 11th Conf. Severe Local Storms, Amer. Meteor. Soc., Boston, 172-176.

Suomi, V.E., Principal Investigator, 1980: Studies of the Atmosphere Using Aerospace Probes, Report on NOAA Grant 04-6-158-44087, SSEC, Madison, WI 53706, 213 pp.

Suomi, V.E., Fox, R.J., Limaye, S., and Smith, W.L., 1983: McIDAS III: A modern interactive data access and analysis system. Accepted for publication by the J. Clim. Appl. Meteor., Amer. Meteor. Soc., Boston, MA.

Umenhofer, T.A., 1975: Overshooting behavior of three tornado producing thunderstorms, Preprint, 9th Conf. Severe Local Storms, Amer. Meteor. Soc., Boston, 96-99.

Acknowledgements

In addition to the authors, work was performed on this project by Arthur Thomas. We would like to thank those people who helped us with data acquisition, particularly Dr. Peter Ray of NSSL, and Drs. Gregory Wilson and James Arnold of MSFC. Typing and other support services were performed by Joanne Edwards and Angela Crowell during the course of the project.

Tables

Figures

Figure 1: a) May 2, 1979, 2314 GMT GOES infrared image with transposed 250 mb cloud tracers (light) and rawinds (dark) from 250 mb. Flags are in ms^{-1}.

b) Same image as a) but with transposed 250 mb streamlines (solid) and isotachs (dashed) in ms^{-1}.

Figure 2: May 2, 1979, 2314 GMT visible image with transposed 925 mb streamlines and isotachs in ms^{-1}.

Figure 3: a) May 2, 1979, 2314 GMT infrared image with transposed contours of 250 mb horizontal divergence (x 10^{-5} s^{-1}).

b) 2314 GMT visible image with 500 mb streamlines and contours of vorticity (x 10^{-5} s^{-1}).

Figure 4: a) May 2, 1979, 2314 GMT visible image with contours of 925 mb divergence.

b) Same as a) but with contours of vorticity.

Figure 5: a) May 2, 1979, 2314 GMT visible image with contours of pressure (mb x 10^{-1}) (dashed) and streamlines (solid) on a 288° theta surface.

b) Same as a) but for moisture divergence (gkg^{-1} s^{-1}) instead of pressure and streamlines.

Figure 6 a) Eight times blowup of the May 2, 1979 severe weather area at 2314 GMT.

b) Same as a) but with brightnesses subjected to a high pass filter.

Figure 7 May 2, 1979, 2311 GMT anvil motion tracks and the tracks of three tornadoes in existence over a two-hour period, labeled T_1 (2215 to 2320 GMT), T_2 (2217 to 2250 GMT), and T_3 (2345 to 2355 GMT). The heavy outline is the anvil boundary.

Figure 8 a) RHI plot, May 2, 1979, 2230 GMT, centered at NSSL

b) Full resolution GOES visible image, May 2, 1979, 2314 GMT, with radar overlaid.

Figure 9: Three-dimensional histogram of 1000 m WSR-57 radar (Norman, OK) vs. GOES 4 km infrared temperatures (°K). 1938 GMT, May 20, 1979.

Figure 10: Same as Fig. 9, except 2314 GMT, May 20, 1979.

Figure 11: Eight times blowup of visible brightness contours from GOES image, 2230 GMT, May 2, 1979. Contour values range from 180 to 200 digital counts. The locations of two tornadoes, T_1 and T_2, are indicated.

Figure 12: Same as Fig. 11, except for satellite derived infrared temperatures (°K).

Figure 13: GOES full resolution visible image for 2230 GMT, May 2, 1979, with tornado and hail locations superimposed.

Figure 14: An operator-drawn area statistics graphics outline enclosing a thunderstorm anvil along with a graphics cursor boundary covering a portion of the inner anvil of a GOES-E visible image at 2114 GMT, May 2, 1979, over central Oklahoma.

Figure 15: IR temperature threshold curves during Storm A over central Oklahoma, May 2, 1979.

Figure 16: IR temperature threshold curves during Storm B over central Oklahoma, May 2, 1979.

Appendix: Data Products Generated for This Project (Available from SSEC)

Satellite Data Tapes

Tape #	DAY(JULIAN)	TIME(GMT)	TIME INTERVAL (MIN)	SENSOR	RES(Mi)
1	140	1730-1756	3	VIS/IR	½/2
892	122	1900-2150	3,6	VIS	½
971	122	2153-2345	6	VIS	½
976	122	2351	-	VIS	½
	123	0000	-	VIS	½
	122	1900-2130	3,6	VIS	1
1000	122	2144-2330	3,6	VIS	1
1053	122	2338-2350	6	VIS	1
	123	0000	-	VIS	1
	122	1900-2123	3,6	IR	2
1060	122	2126-2314	3,6	IR	2
1352	122	1800-2330	30	VIS	2
1353	122	1800-2330	30	IR	2
1354	122	1030-1730	30	VIS	2
1355	122	1030-1730	30	VIS	2
1356	123	0000	-	VIS	2
	140	1430-2100	30	VIS	2
1357	123	0000	-	IR	2
	140	1430-2100	30	IR	2
1358	140	2130-2330	30	VIS	2
	141	0000	-	VIS	2
	159	900-1300	30	VIS	2
1359	140	2130-2330	30	IR	2
	141	0000	-	IR	2

Tape #	DAY(JULIAN)	TIME(GMT)	TIME INTERVAL (MIN)	SENSOR	RES(Mi)
	159	900-1300	30	IR	2
1361	159	1330-2030	30	VIS	2
1362	159	1330-2030	30	IR	2
1363	159	2100-2330	30	VIS/IR	2/2
	160	0000	-	VIS/IR	2/2
1418	122	1911-1923	6	VIS/VIS/IR	½/1/2
	122	2320-2350	6	IR	2
	123	0000	-	IR	2
1419	122	1938-2053	3	VIS	½
1420	140	2056-2200	3	VIS	½
1421	140	1800-2200	3	IR	2
1422	140	1953-2053	3	VIS	½
1423	140	1800-1950	3	VIS	½
2144	122	2144-2238	3	VIS	2

Satellite Data (Brightness Normalized) Tapes

Tape # RES(Mi)	Day(Julian)	TIME(GMT)	TIME INTERVAL (MIN)	SENSOR	
894	122	1930-2053	3,6	VIS	½
895	122	2130-2223	3,6	VIS	½
959	122	2256-2300	6	VIS	½
1437	140	1938-2200	3	VIS	½
1800	140	1800-1756	3	VIS	½

Satellite Data (High Pass Filter) Tape

HIPASS	122	2308-2326	3	VIS	½

Radar Tapes

Tape #	Day(Julian)	Times(GMT)	TIME INTERVAL (MIN)
2024	140	2024-2102	5
2056	122	2056-2151	5
2103	140	2103-2141	5
2156	122	2156-2244	5
2253	122	2253-2341	5

SDS Tapes

Tape #	Type	Day	Times(GMT)	
1	PAM	123	0000-0559	1 min data
	PAM	122	0300-2359	1 min data
	PAM	140	0000-2359	1 min data
	SVR	122	-	
	SVR	140	-	
	SVR	159	-	
	RAO	122;123	0000,1200;0000,1200	Conventional Network
	SVC	122;123	0000-2300;0000-2300	Conventional Network
	SVC	140;141	0000-2300;0000-2300	Conventional Network
	RAO	140;141	0000,1200;0000,1200	Conventional Network
	RAO	122	2000	Vertical profiles from SND files
	RAO	122	2100	Vertical profiles from SND files
	SND	122	2000	TIROS-N Sounding
	SND	122	2100	TIROS-N Sounding
	AC	122	2217-2315	1 sec data QueenAire
	AC	122	2147-2356	1 sec data Sabreliner
SE3600	RAO	122;123	2300;0000-0600	RAOB History tape 2 hourly
PT2308	WIN	122	2311,2327,2323	high pass filter vectors (cloudtop)
PT122	WIN	122	2311,2327,2323	cloud top vectors